

## Abstract

# Measurement of total hadronic differential cross sections in the LArIAT experiment

Elena Gramellini

2018

**6 Abstract goes here. Limit 750 words.**

# **Measurement of total hadronic differential cross sections in the LArIAT experiment**

A Dissertation  
Presented to the Faculty of the Graduate School  
of  
Yale University  
in Candidacy for the Degree of  
Doctor of Philosophy

15 by  
16 Elena Gramellini

<sup>17</sup> Dissertation Director: Bonnie T. Fleming

18 Date you'll receive your degree

<sup>19</sup>

Copyright © 2017 by Elena Gramellini

<sup>20</sup>

All rights reserved.

21

*A mia mamma e mio babbo,*

22

*grazie per le radici e grazie per le ali.*

23

*To my mom and dad,*

24

*thank you for the roots and thank you for the wings.*

# <sup>25</sup> Contents

<sup>26</sup>	<b>Acknowledgements</b>	<b>vi</b>
<sup>27</sup>	<b>0 Liquid Argon Detectors at the Intensity Frontier</b>	<b>1</b>
<sup>28</sup>	0.1 The Liquid Argon Time Projection Chamber Technology . . . . .	1
<sup>29</sup>	0.1.1 TPCs, Neutrinos & Argon . . . . .	1
<sup>30</sup>	0.1.2 LArTPC: Principles of Operation . . . . .	5
<sup>31</sup>	0.1.3 Liquid Argon: Ionization Charge . . . . .	6
<sup>32</sup>	0.1.4 Liquid Argon: Scintillation Light . . . . .	12
<sup>33</sup>	0.1.5 Signal Processing and Event Reconstruction . . . . .	16
<sup>34</sup>	0.2 The Intensity Frontier Program . . . . .	20
<sup>35</sup>	0.2.1 Prospects for LArTPCs in Neutrino Physics: SBN and DUNE	20
<sup>36</sup>	0.2.2 Prospects for LArTPCs in GUT Physics: DUNE . . . . .	22
<sup>37</sup>	0.2.3 Enabling the next generation of discoveries: LArIAT . . . . .	23
<sup>38</sup>	<b>1 Total Hadronic Cross Section Measurement Methodology</b>	<b>26</b>
<sup>39</sup>	1.1 Event Selection . . . . .	27
<sup>40</sup>	1.1.1 Selection of Beamline Events . . . . .	27
<sup>41</sup>	1.1.2 Particle Identification in the Beamline . . . . .	28
<sup>42</sup>	1.1.3 TPC Selection: Halo Mitigation . . . . .	28
<sup>43</sup>	1.1.4 TPC Selection: Shower Removal . . . . .	29
<sup>44</sup>	1.2 Beamline and TPC Handshake: the Wire Chamber to TPC Match .	30

45	1.3	The Thin Slice Method . . . . .	32
46	1.3.1	Cross Sections on Thin Target . . . . .	32
47	1.3.2	Not-so-Thin Target: Slicing the Argon . . . . .	33
48	1.3.3	Corrections to the Raw Cross Section . . . . .	35
49	1.4	Procedure testing with truth quantities . . . . .	36
50	<b>2</b>	<b>Preparatory Work</b>	<b>38</b>
51	2.1	Cross Section Analyses Data Set . . . . .	38
52	2.2	Construction of a Monte Carlo Simulation for LArIAT . . . . .	40
53	2.2.1	G4Beamline . . . . .	40
54	2.2.2	Data Driven MC . . . . .	44
55	2.2.3	Estimate of Energy Loss before the TPC . . . . .	47
56	2.3	Tracking Studies . . . . .	50
57	2.3.1	Study of WC to TPC Match . . . . .	51
58	2.3.2	Tracking Optimization . . . . .	54
59	2.3.3	Angular Resolution . . . . .	54
60	2.4	Calorimetry Studies . . . . .	58
61	2.4.1	Energy Calibration . . . . .	58
62	2.4.2	Kinetic Energy Measurement . . . . .	60
63	<b>3</b>	<b>Negative Pion Cross Section Measurement</b>	<b>64</b>
64	3.1	Raw Cross Section . . . . .	64
65	3.1.1	Statistical Uncertainty . . . . .	65
66	3.1.2	Treatment of Systematics . . . . .	68
67	3.2	Corrections to the Raw Cross Section . . . . .	68
68	3.2.1	Background subtraction . . . . .	68
69	3.2.2	Efficiency Correction . . . . .	68
70	3.2.3	Final Plots . . . . .	68

# <sup>71</sup> Acknowledgements

<sup>72</sup>                   “*Dunque io ringrazio tutti quanti.*

<sup>73</sup>                   *Specie la mia mamma che mi ha fatto così funky.”*

<sup>74</sup>                   – Articolo 31, Tanqi Funky, 1996 –

<sup>75</sup>                   “*At last, I thank everyone.*

<sup>76</sup>                   *Especiallly my mom who made me so funky.”*

<sup>77</sup>                   – Articolo 31, Tanqi Funky, 1996 –

<sup>78</sup>         A lot of people are awesome, especially you, since you probably agreed to read

<sup>79</sup>     this when it was a draft.

<sup>80</sup> **Chapter 0**

<sup>81</sup> **Liquid Argon Detectors at the**  
<sup>82</sup> **Intensity Frontier**

<sup>83</sup> In the next few years, LArTPCs will be the tools to answer some of the burning  
<sup>84</sup> questions in neutrino physics today. This section illustrates the operational principles  
<sup>85</sup> of this detector technology, as well as the scope of the key detectors in the US liquid  
<sup>86</sup> argon program – SBN, DUNE and LArIAT.

<sup>87</sup> **0.1 The Liquid Argon Time Projection Chamber**  
<sup>88</sup> **Technology**

<sup>89</sup> **0.1.1 TPCs, Neutrinos & Argon**

<sup>90</sup> David Nygren designed the first Time Projection Chamber (TPC) in the late 1970s [41]  
<sup>91</sup> for the PEP-4 experiment, a detector apt to study electron-positron collisions at the  
<sup>92</sup> PEP storage ring at the SLAC National Accelerator Laboratory. From the original  
<sup>93</sup> design in the seventies – a cylindrical chamber filled with methane gas – the TPC  
<sup>94</sup> detector concept has seen many incarnations, the employment of several different  
<sup>95</sup> active media and a variety of different particle physics applications, including, but

96 not limited to the study of electron/positron storage rings (e.g. PEP4, TOPAZ,  
97 ALEPH and DELPHI), heavy ions collisions in fixed target and collider experiments  
98 (e.g. EOS/HISSL and ALICE ), dark matter (ArDM), rare decays and capture (e.g.  
99 TRIUMF, MuCap), neutrino detectors and nucleon decay (ICARUS, SBN, DUNE),  
100 and neutrino less double beta decay (Next). A nice review of the history of TPCs  
101 and working principles is provided in [31].

102 Several features of the TPC technology make these detectors a more versatile tool  
103 compared to other ionization detectors and explain such a wide popularity. TPCs are  
104 the only electronically read detector which deliver simultaneous three-dimensional  
105 track information and a measurement of the particle energy loss. Leveraging on both  
106 tracking and calorimetry, particle identification (PID) capabilities are enhanced over  
107 a wide momentum range.

108 Historically, the active medium in ionization detectors has been in the gaseous  
109 form. Carlo Rubbia first proposed the use of a Liquid Argon TPC for a neutrino  
110 experiment, ICARUS [46], in 1977. Using nobles elements in the liquid form for  
111 neutrino detectors is advantageous for several reasons. The density of liquids is  $\sim$ 1000  
112 times greater than gases, augmenting the number of targets for neutrino's interaction  
113 in the same volume, in a effort to balance the smallness of neutrino cross section.  
114 Since the energy loss of charged particle is proportional to the target material density,  
115 as shown in the Bethe-Block equation (eq. 1), the increased density reflects into a  
116 proportionally higher energy loss, enhancing the calorimetry capability of detectors  
117 with a liquid active medium. Additionally, the ionization energy of liquids is smaller  
118 than gasses by the order of tens of eV. Thus, at the passage of charged particles,  
119 liquids generally produce more ionization electrons than gases for the same deposited  
120 energy, forcing the particles to deposit more energy in a shorter range. The downside  
121 of using noble liquid elements in experiments is that they require expensive cryogenic  
122 systems to cool the gas until it transitions to its the liquid form. The properties

Element	LAr	LXe
Atomic Number	18	54
Atomic weight A	40	131
Boiling Point Tb at 1 atm	87.3 K	165.0 K
Density	1.4 g/cm <sup>3</sup>	3.0 g/cm <sup>3</sup>
Radiation length	14.0 cm	2.8 cm
Moliere Radius	10.0 cm	5.7 cm
Work function	23.6 eV	15.6 eV
Electron Mobility at $E_{field} = 10^4$ V/m	0.047 m <sup>2</sup> /Vs	0.22 m <sup>2</sup> /Vs
Average dE/dx MIP	2.1 MeV/cm	3.8 MeV/cm
Average Scintillation Light Yield	40000 $\gamma$ /MeV	42000 $\gamma$ /MeV
Scintillation $\lambda$	128 nm	175 nm

Table 1: LAr, LXe summary of properties relevant for neutrino detectors.

123 of liquid argon in comparison liquid xenon – a popular choice for dark matter and  
 124 neutrinoless double beta decay detectors – are summarized in table 1. Albeit xenon  
 125 would be more desirable than argon given some superior properties such as lower  
 126 ionization energy and higher density and light yield, argon relative abundance abates  
 127 the cost of argon compared to xenon, making argon a more viable choice for the  
 128 construction of ton (and kilo-ton) scale neutrino detectors.

129 LArTPCs are some times referred as to “electronic” bubble-chambers, for the  
 130 similarity in the tracking and energy resolution which is coupled with an electronic  
 131 readout of the imaging information in LArTPCs. Compared to these historic detectors  
 132 however, LArTPC bestow tridimensional tracking and a self triggering mechanism  
 133 provided by the scintillation light in the liquid argon. An event display of a  $\nu_\mu$  CC  
 134 interaction candidate in the MicroBooNE detector is shown in picture 1 to display  
 135 the level of spatial details these detectors are capable of; the color scale of the image  
 136 is proportional to the energy deposited, hinting to these calorimetry capabilities of  
 137 the detectors.

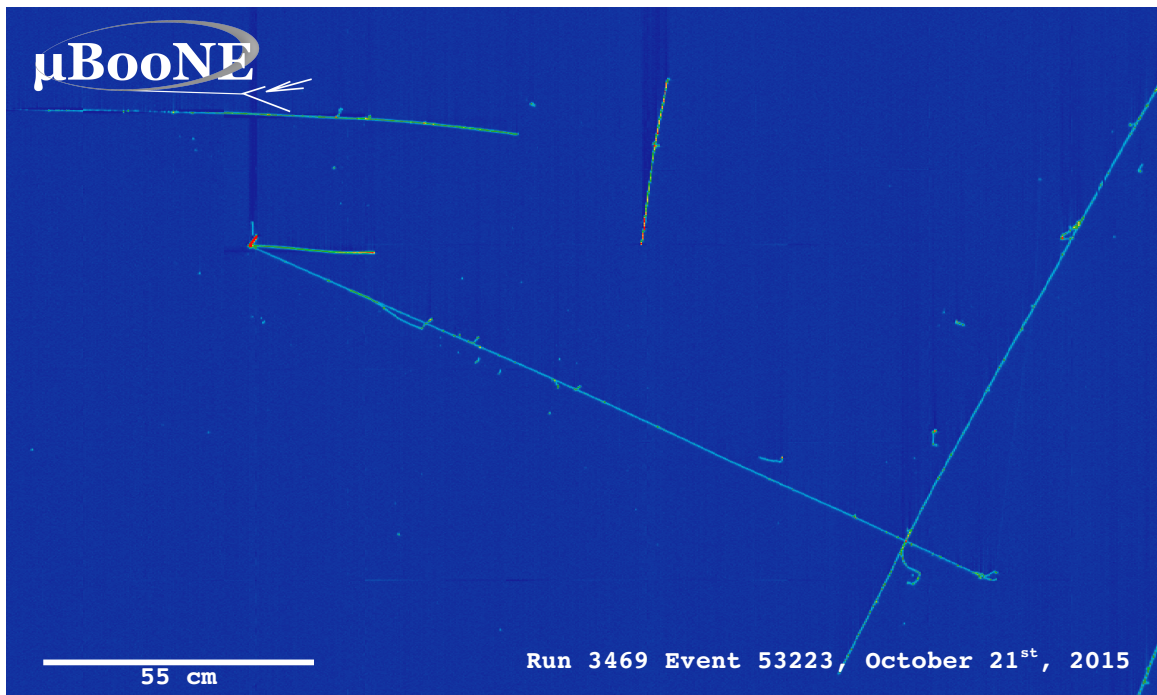


Figure 1: Event display of a  $\nu_\mu$  CC interaction candidate in the MicroBooNE detector.

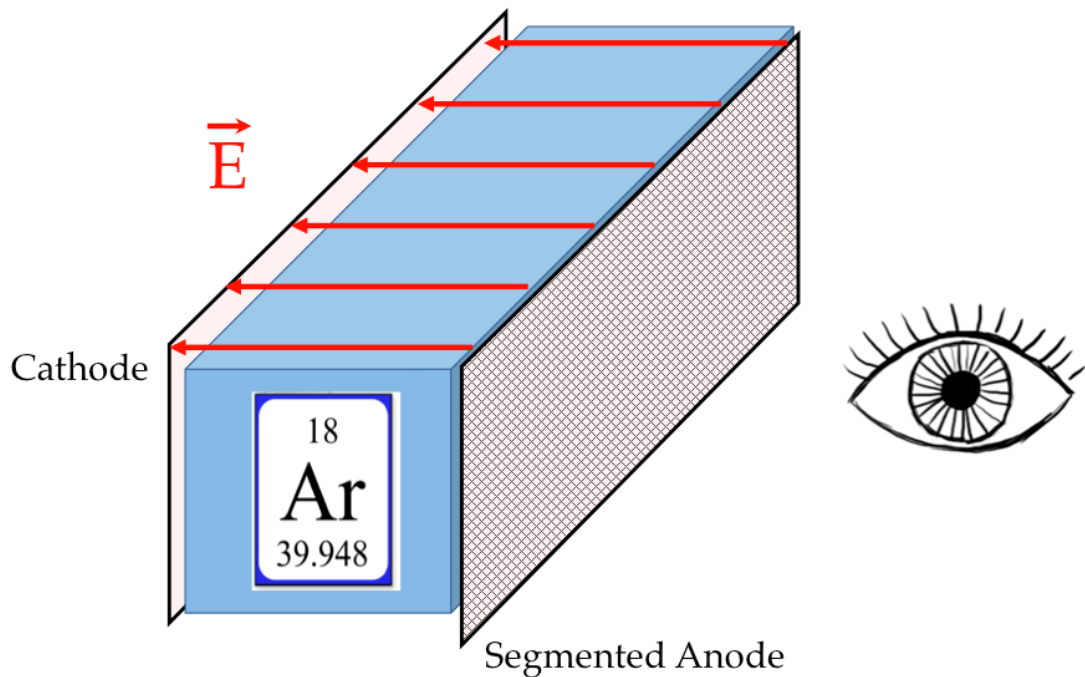


Figure 2: A cartoonish sketch of a LArTPC.

138 **0.1.2 LArTPC: Principles of Operation**

139 To the bare bones, a LArTPC is a bulk of liquid argon sandwiched in a flat capac-  
140 itor, equipped with a light collection system, as the cartoon in 2 shows. A uniform  
141 electric field of the order of 500 V/cm is maintained constant between the faces of the  
142 capacitor. The anode is sensitive to ionization charge and it is usually made of two  
143 or more planes segmented into several hundreds parallel sense wires a few millimeters  
144 apart; different geometries for the anode segmentation are under study [24].

145 Argon ionization and scintillation are the processes leveraged to detect particles  
146 in the LArTPC active volume. When a ionizing radiation traverses the argon active  
147 volume it leaves a trail of ionization electrons along its trajectory and it excites  
148 the argon producing scintillation light – details on the production and detection of  
149 ionization charge and scintillation light are provided in 0.1.4 and 0.1.4 respectively.

150 The optical detector sees the argon scintillation light in matters of nanoseconds.  
151 This flash of light determines the start time of an event in the chamber,  $t_0$ . The  
152 uniform electric field drifts the ionization electrons from the production point towards  
153 the anode in order of hundreds of microseconds or more depending on the chamber  
154 dimensions<sup>1</sup>. The anode sense wires see either an induced current by the drifting  
155 ionization charge (on induction planes) or an injection of such charge (collection  
156 plane). An appropriate choice of the voltage bias on each wire plane assures ideal  
157 charge transparency, so that all the ionization charge is collected on the collection  
158 plane and none on the induction planes.

159 The arrival time of the charge on the anode sense wires is used to measure the  
160 position of the original ionizing radiation in the drift direction. In fact, since the  
161 constant electric field implies that the drift velocity is also constant, the position of

---

1. The ionized argon also drifts, but in the opposite directions compared to the electrons. Since the drift time is proportional to the particle mass, the ions' drift time is much longer than the electrons'. Ionized argon is collected on the cathode which is not instrumented, so it is not used to infer information about the interactions in the chamber.

162 the original ionization is simply given by the multiplication of the drift velocity by the  
 163 drift time, where the “drift time” is the difference between  $t_0$  and the charge arrival  
 164 time on the wire planes. The spacial resolution on this dimension is limited by the  
 165 time resolution of the electronics or by longitudinal diffusion of the electrons. The  
 166 spatial information on the different wire planes maps a bi-dimensional projection of  
 167 the interaction pattern in the plane perpendicular to the drift direction. The spacial  
 168 resolution on this dimension is limited by the transverse electron diffusion in argon  
 169 and by the grain of the anode segmentation, i.e. the spacing between the wires in  
 170 the sense planes [23]. The off-line combination of the 2-D information on the wire  
 171 planes with the timing information allows for the 3D reconstruction of the event in  
 172 the chamber.

173 Since the charge deposited by the ionizing radiation is proportional to the de-  
 174 posited energy and the charge collected on the sense plane is a function of the de-  
 175 posited charge, LArTPCs allow the measurement of the energy deposit in the active  
 176 volume. Effects due to the presence of free charge and impurities in the active vol-  
 177 ume, such as a finite electron lifetime, recombination and space charge, complicate  
 178 the relationship between deposited and collected charge affecting the measurement of  
 179 the particle’s energy, as described in the next section.

### 180 **0.1.3 Liquid Argon: Ionization Charge**

181 The mean rate of energy loss by moderately relativistic elementary charge particles  
 182 heavier than electrons is well described by the modified Bethe-Bloch [43] equation

$$-\frac{dE}{dx} = K z^2 \frac{Z}{A} \varrho \frac{1}{\beta^2} \left[ \frac{1}{2} \ln \frac{2m_e c^2 \beta^2 \gamma^2 T_{max}}{I^2} - \beta^2 - \frac{\delta}{2} \right], \quad (1)$$

183 where  $z$  is the number of unit charge of the ionizing radiation,  $Z$ ,  $A$  and  $\varrho$  are the  
 184 atomic number, mass number and density of the medium,  $m_e$  is the electron mass,

185  $\gamma = \frac{\beta}{\sqrt{1-\beta^2}}$  is the Lorentz factor of the ionizing radiation,  $T_{max}$  is the maximum kinetic  
 186 energy which can be imparted to a free electron in a single collision,  $I$  is the mean  
 187 excitation energy on eV,  $\delta$  is the density correction and  $K = 0.307075 \text{ MeV g}^{-1} \text{ cm}^2$  is  
 188 a numerical conversion factor. The Bethe-Bloch treats the energy loss by an ionizing  
 189 radiation via quantum-mechanical collisions producing ionization or an excitation in  
 190 the medium as an uniform and continuous process. The density correction terms  
 191 becomes relevant for incident particle with high energy, where screening effects due  
 192 to the polarization of the medium by high energy particles occur.

193 Excitation and ionization of the detector medium occur in similar amounts. Since  
 194 the ionizing collisions occur randomly, we can parametrize their number  $k$  in a segment  
 195 of length  $s$  along the track with a Poissonian function

$$P(k) = \frac{s^k}{k! \lambda^k} e^{-s/\lambda}, \quad (2)$$

196 where  $\lambda = 1/N_e \sigma_i$ , with  $N_e$  being the electron density of  $\sigma_i$  the ionization cross-  
 197 section per electron. About 66% of the ionizing collisions in Argon produce only  
 198 a single electron/ion pair [31]; in the other cases, the transferred kinetic energy is  
 199 enough for the primary electron to liberate one or more secondary electrons, which  
 200 usually stay close to the original pair. Occasionally, electrons can receive enough  
 201 energy to be ejected with high energy, forming a so-called “ $\delta$ -ray”: a detectable short  
 202 track off the particle trajectory, as shown in figure 3. The average number of  $\delta$ -ray  
 203 with energy  $E > E_0$  per cm follows the empirical form

$$P(E > E_0) \sim \frac{y}{\beta^2 E_0}, \quad (3)$$

204 where  $y$  is an empirical factor depending on the medium (0.114 for gaseous Ar), and  
 205  $\beta$  is  $v/c$ .

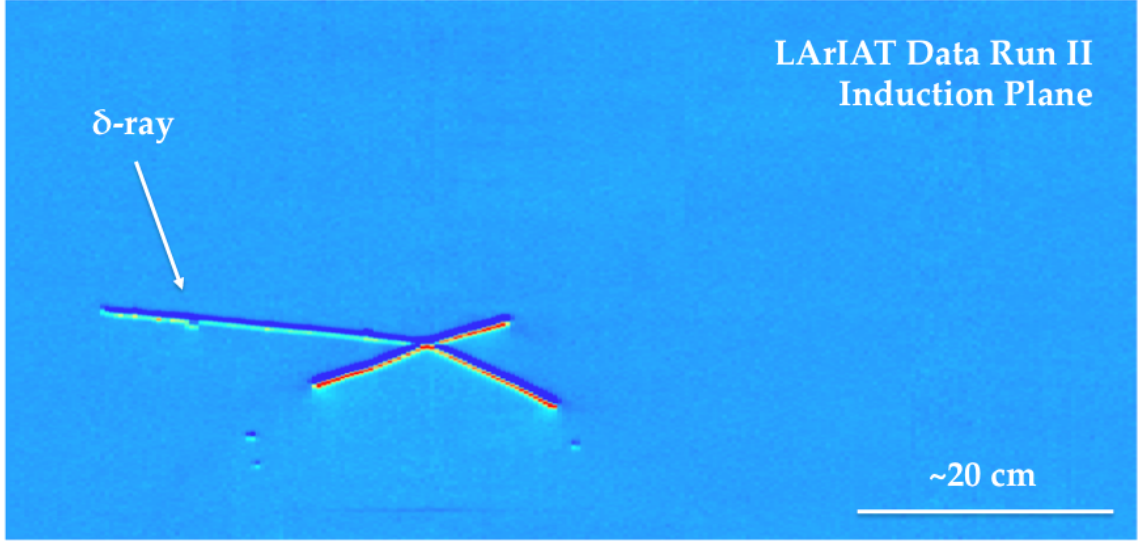


Figure 3: Events display for a LArIAT pion absorption candidate on the induction plane, with highlighted delta ray.

## 206 Purity & Electron Life Time

207 The presence of electronegative contaminants in liquid argon, such as oxygen  $O_2$   
208 and water  $H_2O$ , is particularly pernicious, since these molecules quench the charge  
209 produced by the ionizing radiation. Thus, amount of charge per unit of length  $dQ/dx$   
210 collected on the collection plane depends on the charge's production point in the  
211 detector: ionization produced close to the cathode will see more impurities along its  
212 journey to the collection plane than ionization produced close to the anode, resulting  
213 in greater attenuation of its charge. As a result, the amount of charge collected on  
214 the sense wires as a function of the traveled distance follows an exponential decay  
215 trend. The traveled distance is generally measured in terms of drift time and the  
216 characteristic time constant of the exponential decay is called electron lifetime  $\tau_e$ .  
217 Figure 4 shows the typical life time for LArIAT data. The procedure to measure  
218 the electron lifetime in LArIAT is outlined in [45]. LArIAT small drift distance (47  
219 cm) allows for a relatively short electron life time. The life time for bigger detectors  
220 such as MicroBooNE, whose drift distance is 2.6 m, needs to be of the order of  
221 tens of milliseconds to allow a charge collection usable for physics analyses. Energy

222 reconstruction in LArTPC applies a correction for the finite lifetime to calibrate the  
223 detector calorimetric response; details for LArIAT are provided in Section 2.4.1.

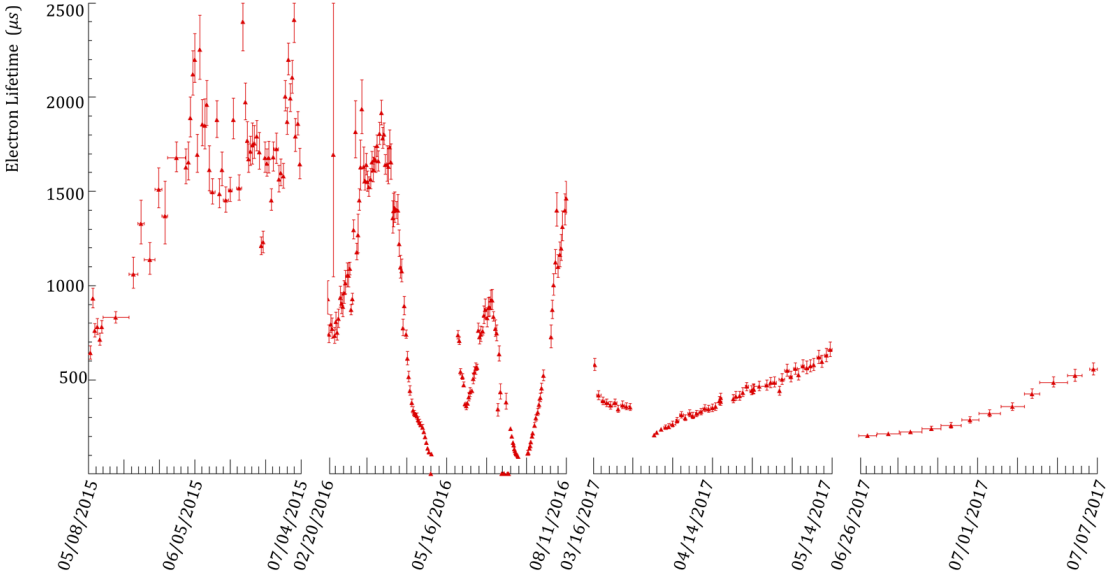


Figure 4: Electron lifetime during the LArIAT run period [22].

224 LArTPCs use hermetically sealed and leak-checked vessels to abate the leakage  
225 and diffusion of contaminants into the system. The liquid argon filling of the vol-  
226 ume occurs after the vessel is evacuated or purged with gaseous argon [6] to reduce  
227 remaining gases in the volume. Even so, the construction of a pure tank of argon is  
228 unviable, as several sources of impurity remain. In particular, impurities can come  
229 from the raw argon supply, the argon filtration system and from the outgassing from  
230 internal surfaces. Outgassing is a continuous diffusive process producing contami-  
231 nants, especially water, even after the vessel is sealed, particularly from materials in

232 the ullage region<sup>2</sup>. Since research-grade argon comes from the industrial distillation  
233 of air, the impurities with the highest concentration are nitrogen, oxygen and water,  
234 generally maintained under the 1 part per million level by the vendor. Even so, a  
235 higher level of purity is necessary to achieve a free electron life time usable in meter  
236 scale detectors. Thus, argon is constantly filtered in the cryogenic system, which  
237 reduce the oxygen and water contamination to less than 100 parts per trillion. The  
238 filtration system depends on the size and drift distance of the experiment and, for  
239 experiments on several meters scale, it includes an argon recirculation system.

#### 240 Recombination Effect

241 After production, ionization electrons thermalize with the surrounding medium and  
242 may recombine with nearby ions. Recombination might occur either between the  
243 electron and the parent ion through Coulomb attraction, as described in the geminate  
244 theory [42], or thanks to the collective charge density of electrons and ions from  
245 multiple ionizations in a cylindrical volume surrounding the particle trajectory, as  
246 described in the columnar model [34]. Consideration on the average electron-ion  
247 distance and the average ion-ion distance for argon show that the probability of  
248 geminate recombination is low; thus recombination in argon is mainly due to collective  
249 effects [2]. Since protons, kaons and stopping particles present a higher ionization  
250 compared to MIPs, recombination effects are more prominent when considering the  
251 reconstruction of energy deposited by these particles.

252 Theoretical descriptions of recombination based on the Birks model and the Box  
253 model are provided in [18] and [48], respectively. The Birks model assumes a gaussian  
254 spatial distribution around the particle trajectory during the entire recombination  
255 phase and identical charge mobility for ions and electrons. The Box model also as-

---

2. While the liquid argon low temperature reduces outgassing in the liquid, this process remains significant for absorptive material (such as plastic) above the surface of the liquid phase.

sumes that electron diffusion and ion mobility are negligible in liquid argon during recombination. In these models, the fraction of ionization electrons surviving recombination is a function of the number of ion-electron pairs per unit length, the electric field, the average ion-electron separation distance after thermalization and the angle of the particle with respect to the direction of the electric field – plus the diffusion coefficient in the Birks model. Given the stringent assumptions, it is perhaps not surprising that these models are in accordance to data only in specific regimes: the Birks model is generally used to describe recombination for low  $dE/dx$ , the Box model for high  $dE/dX$ . In LArTPC, the ICARUS and ArgoNeut experiments have measured recombination in [11] and [2] respectively. Since LArIAT uses the refurbished ArgoNeut TPC and cryostat at the same electric field, LArIAT currently corrects for recombination using the ArgoNeut measured recombination parameters in [2].

## Space Charge Effect

Slow-moving positive argon ions created during ionization can build-up in LArTPC, causing the distortion of the electric field within the detector. This effect, called “space charge effect” leads to a displacement in the reconstructed position of the signal ionization electrons. In surface LArTPCs the space charge effect is primarily due to the rate of ionization produced by cosmic rays which is slowly drifting in the chamber at all times. Surface LArTPC of the size of several meters are expected to be modestly impacted from the space charge effect, where charge build-up create anisotropy of the electric field magnitude of the order of 5% at a drift field of 500 V/cm [39]. The smallness of the LArIAT drift volume and its relatively high electric field are such that the effect of space charge is expected to be negligible.

<sup>279</sup> **0.1.4 Liquid Argon: Scintillation Light**

<sup>280</sup> Liquid argon emits scintillation light at the passage of charged particles. LArTPCs  
<sup>281</sup> leverage this property to determine when the ionization charge begins to drift towards  
<sup>282</sup> the anode plane.

<sup>283</sup> **Scintillation Process**

<sup>284</sup> Scintillation light in argon peaks in the ultraviolet at a 128 nm, shown in comparison  
<sup>285</sup> to Xenon and Kypton in Figure 5, from [40]. The light yield collected by the optical  
<sup>286</sup> detector depends on the argon purity, the electric field, the  $dE/dx$  and particle type,  
<sup>287</sup> averaging at the tens of thousands of photons per MeV.

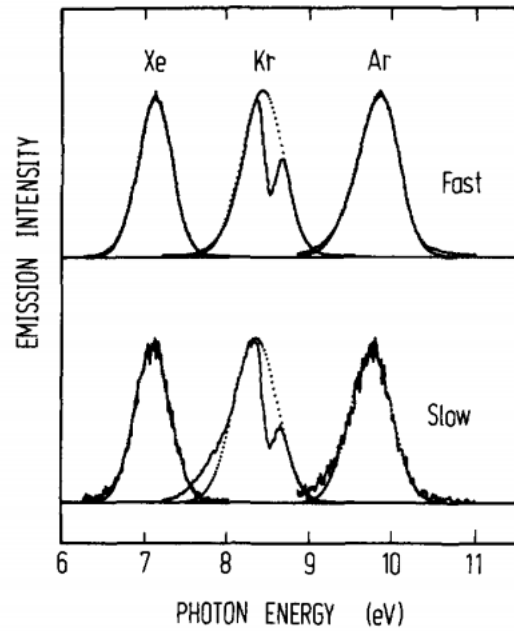


Figure 5: Emission spectra of the fast and slow emission components in Xenon, Krypton and Argon according to [40]. The dotted lines correspond to the Gaussian fits.

<sup>288</sup> The de-excitation of Rydberg dimers in the argon is responsible for the scintillation  
<sup>289</sup> light. Rydberg dimers exist in two states: singlets and a triplets. The time constant  
<sup>290</sup> for the singlet radiative decay is 6 ns, resulting in a prompt component for the scin-

291 tillation light. The decay of the triplet is delayed by intersystem crossing, producing  
292 a slow component with a time constant of  $\sim$  1500 ns. “Self-trapped exciton lumines-  
293 cence” and “recombination luminescence” are the two processes responsible for the  
294 creation of the Rydberg dimers [36]. In the first process, a charged particle excites an  
295 argon atom which becomes self-trapped in the surrounding bulk of argon, forming a  
296 dimer; the dimer is in the singlet state 65% of the times and in the triplet state 35%  
297 of the times. In case of recombination luminescence, the charged particle transfers  
298 enough energy to ionize the argon. The argon ion forms a charged argon dimer state,  
299 which quickly recombines with the thermalized free electron cloud. Excimer states  
300 are produced in the recombination, roughly half in the singlet and half in the triplet  
301 state. The light yield dependency on the electric field, on the  $dE/dx$  and particle  
302 type derives from the role of free charge in the recombination luminescence process.  
303 The spacial separation between the argon ions and the free electron cloud depends on  
304 the electric field. On one hand, a strong electric field diminishes the recombination  
305 probability, leading to a smaller light yield; on the other, it increases the free charge  
306 drifting towards the anode plane. Hence, the amount of measurable charge and light  
307 anti-correlates as a function of the electric field. Ionizing particles in the argon mod-  
308 ify the local density of both free electrons and ions depending on their  $dE/dx$ . Since  
309 the recombination rate is proportional to the square of the local ionization density,  
310 highly ionizing particles boost recombination and the subsequent light yield compared  
311 to MIPs. The possibility to leverage this dependency for pulseshape-based particle  
312 identification has been shown in [19,38].

### 313 Effects Modifying the Light Yield

314 The production mechanism through emission from bound excimer states implies that  
315 argon is transparent to its own scintillation light. In fact, the photons emitted from  
316 these metastable states are not energetic enough to re-excite the argon bulk, greatly

317 suppressing absorption mechanisms. In a LArTPC however, several processes modify  
318 the light yield in between the location where light is produced and the optical detector.  
319 In a hypothetical pure tank of argon, Rayleigh scattering would be the most important  
320 processes modifying the light yield. Rayleigh scattering changes the path of light  
321 propagation in argon, prolonging the time between light production and detection.  
322 The scattering length has been measured to be 66 cm [32] , shorter than the theoretical  
323 prediction of  $\sim$  90 cm [47]; this value is short enough to be relevant for the current  
324 size of LArTPCs detectors. In fact, Rayleigh scattering worsen the resolution on  $t_0$ ,  
325 the start time for charge drifting, and alters the light directionality, complicating the  
326 matching between light and charge coming from the same object in case of multiple  
327 charged particles in the detector.

328 Traces of impurities in argon such as oxygen, water and nitrogen also affect the  
329 light yield, mainly via absorption and quenching mechanisms. Absorption occurs as  
330 the interaction of a 128 nm photon directly with the impurity dissolved in the liquid  
331 argon. Differently, quenching occurs as the interaction of an argon excimer and an  
332 impurity, where the excimer transfers its excitation to the impurity and dissociates  
333 non-radiatively. Given this mechanism, it is evident how quenching is both a function  
334 of the impurity concentrations and the excimer lifetime. Since the triplet states  
335 live much longer than the singlet states, quenching occurs mainly on triplet states,  
336 affecting primarily the slow component of the light, reducing the scintillation yield  
337 and a shortening of the scintillation time constants.

338 The stringent constraints for the electron life time limit the presence of oxygen and  
339 water to such a low level that both absorption and quenching on these impurity is not  
340 expected to be significant. Contrarily, the nitrogen level is not bound by the electron  
341 life time constraints – nitrogen being an inert gas, expensive to filter. Thus, nitrogen  
342 is often present at the level provided by the vendor. The effects of nitrogen on argon  
343 scintillation light have been studied in the WArP R&D program and at several test

344 stands. The quenching process induced by nitrogen in liquid Ar has been measured  
345 to be proportional to the nitrogen concentration, with a rate constant of  $\sim 0.11$   
346  $\mu\text{s}^{-1}$  ppm $^{-1}$ ; appreciable decreasing in lifetime and relative amplitude of the slow  
347 component have been shown for contamination as high as a few ppm of nitrogen [3].  
348 For a nitrogen concentration of 2 parts per million, typical of the current generation  
349 of LArTPC, the attenuation length due to nitrogen has been measured to be  $\sim 30$   
350 meters [35].

### 351 **Wavelength Shifting of LAr Scintillation Light**

352 Liquid argon scintillation light is invisible for most optical detectors deployed in a  
353 LArTPC, such as cryogenic PMTs and SiPMs, since a wavelength of 128 nm is gen-  
354 erally too short to be absorbed from most in glasses, polymers and semiconductor  
355 materials. Research on prototype SiPMs absorbing directly VUV light and their  
356 deployment in noble gasses experiment is ongoing but not mature [49]. Thus, ex-  
357 periments need to shift the wavelength of scintillation light to be able to detect it.  
358 Albeit deployed in different ways, neutrinos and dark matter experiments commonly  
359 use 1,1,4,4-tetraphenyl-butadiene (TPB) to shift the scintillation light. TPB absorbs  
360 the vacuum ultraviolet (VUV) light and emits in the visible at  $\sim 425$  nm [20], with  
361 a ratio of visible photon emitted per VUV photon absorbed of  $\sim 1.2:1$  [28].

362 Neutrino experiments typically coat their optical detector system evaporating a  
363 layer of TPB either directly on the PMTs glass surface or on acrylic plates mounted in  
364 front of the PMTs [26]; this technique allows the fast detection light coming directly  
365 from the neutrino interaction. Dark matter experiments typically evaporate TPB on  
366 reflective foils mounted on the inside walls of the sensitive volume and detect the  
367 light after it has been reflected; this technique leads to a higher and more uniform  
368 light yield, though scattering effects for both the visible and VUV light augment  
369 the propagation time and hinder directionality information [27]. In order to take

370 advantage of both these techniques, hybrid systems with PMT coating and foils are  
371 being considered for the next generation of large neutrino detectors.

### 372 0.1.5 Signal Processing and Event Reconstruction

373 In this section we illustrate the processing and reconstruction chain of the TPC sig-  
374 nals, from the pulses on the sense wire to the construction of three dimensional objects  
375 with associated calorimetry. Different experiments can chose different software pack-  
376 ages for their off line signal processing and event reconstruction, but a popular choice  
377 for US based LArTPCs is LArSoft [21]. Based on the Art framework [30], LArSoft is  
378 an event-based toolkit to perform simulation, analysis and reconstruction of LArT-  
379 PCs events.

380

381 LArTPC signal processing develops in several consecutive stages that we summa-  
382 rize here in the following categories: *Deconvolution*, *Hit Reconstruction*, *2D Cluster-*  
383 *ing*, *3D Tracking*, *Calorimetry Reconstruction*. A visualization of the signal processing  
384 workflow is shown in figure 6.

385

386 **Deconvolution.** Induction and collection planes have different field responses,  
387 given the different nature of the signals on these planes: the wires on the induction  
388 planes see the inductive signal of the drifting charge, while the wires on the collection  
389 planes see the current derived from the charge entering the conductor. Thus, signals  
390 on the induction plane are bi-polar pulse and signal on the collection plane are unipo-  
391 lar pulses, see Figure 6 panel a). The first step in signal processing is deconvolution,  
392 that is a series of off-line algorithms geared towards undoing the detector effects. The  
393 result of the deconvolution step is the production of a comparable set waveforms on  
394 all planes presenting unipolar, approximately gaussian-like pulses (Figure 6 panel b).  
395 Signal from all planes are treated on equal footage beyond this point. Some LArTPC

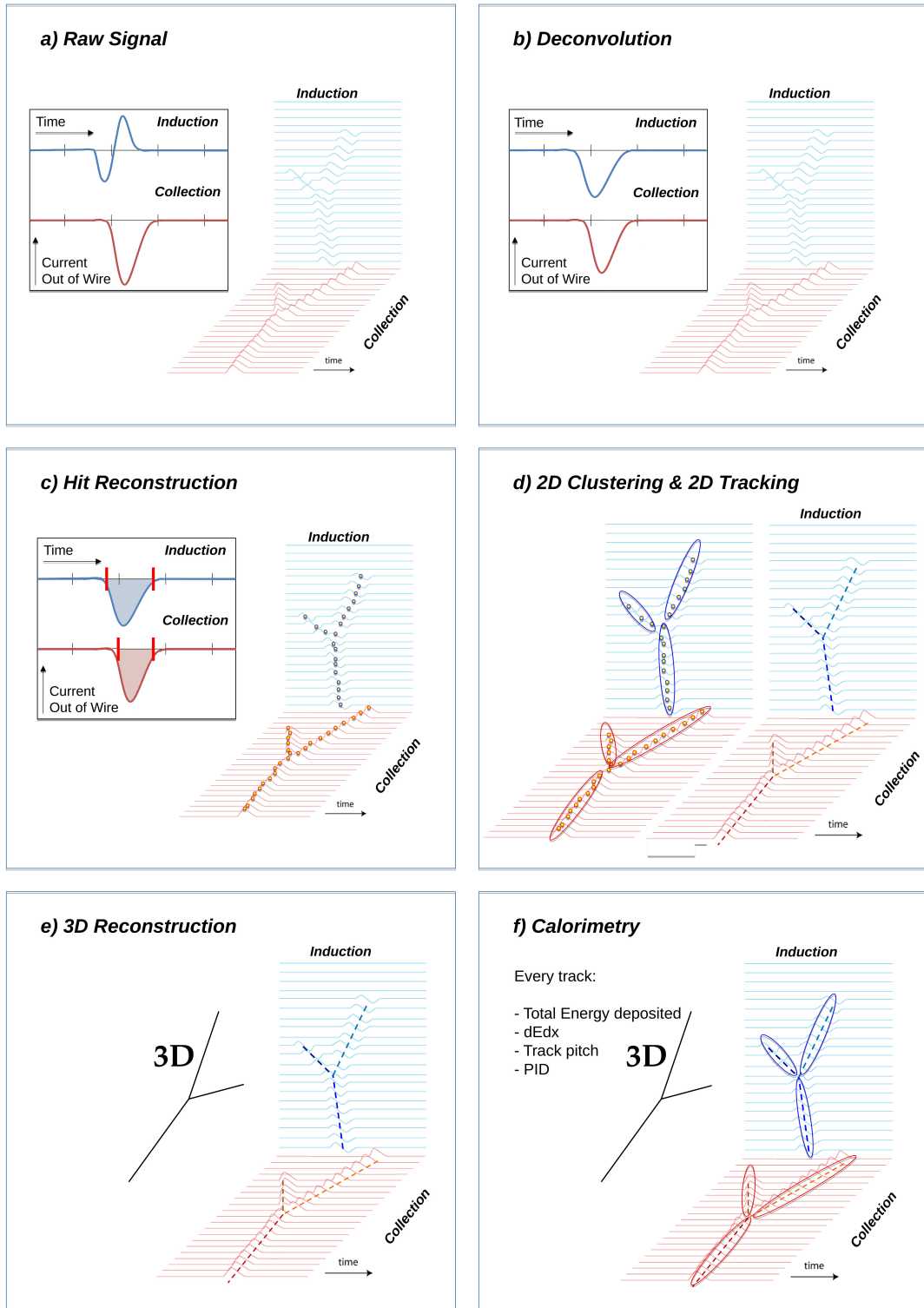


Figure 6: A scheme of a typical signal processing workflow in LArSoft.

396 apply noise filtering in the frequency domain just after the deconvolution to clean  
397 up wire cross talk. Since signals from the LArIAT TPC are extremely clean, noise  
398 filtering is not necessary.

399

400 **Hit Reconstruction.** The second stage of the signal processing is the recon-  
401 struction of hits, indicating an energy deposition in the detector. A peak finder scans  
402 the deconvolved TPC waveforms for each wire on the whole readout time looking for  
403 spikes above the waveform’s baseline. It then fits these peaks with gaussian shapes  
404 and stores the fit parameters such as the quality of the fit, the peak time, height  
405 and area under the gaussian fit. The information resulting from this process on a  
406 single spike form a single reconstructed “hit”, see Figure 6 panel c). The next steps  
407 in the event reconstruction chain will then decide if rejecting hits with poor fits. It  
408 is important to notice how the height and width of the hit depend on the topology  
409 of the event: for example, a particle running parallel to the wire planes will leave  
410 a series of sharp hits on many consecutive wires, while a particle traveling towards  
411 the planes will leave a long, wide hit on very few wires. The height of the hits and  
412 their integral is proportional to the charge collected on the wire, so it depends on the  
413 particle type.

414

415 The event reconstruction chain uses collection of hits to form more complex objects  
416 associated with the particles in the detector. The development of different approaches  
417 to accomplish this task is an extremely hot topic in LArTPC event reconstruction  
418 which spans from more traditional approaches such as line-clustering [17] to the use of  
419 machine learning tools [25]. Generally speaking, the scope of hit clustering and event  
420 reconstruction to provide shower-like or track like-objects with an associated energy  
421 reconstruction. This is because different particles have different topology in the de-  
422 tector – electrons and photon create electromagnetic showers, resulting in shower-like

423 topologies, while muons and hadrons leave track-like signals. For the scope of these  
424 thesis, we will describe only LArIAT’s approach to track reconstruction even if we  
425 recognize the breath of LArTPC event reconstruction is much wider. We are inter-  
426 ested in the reconstruction of pions and kaons in the active volume, whose topology  
427 is track-like.

428

429 **2D Clustering Reconstruction.** The LArIAT reconstruction of track-like ob-  
430 jects starts by clustering hits on the collection and induction planes separately with  
431 the use of the TrajCluster clustering package [16]. TrajCluster looks for a collection  
432 of hits in the wire-time 2D space which can be described with a line-like 2D trajec-  
433 tory. TrajCluster reconstructs trajectories by adding trajectory points to the leading  
434 edge of the trajectory while stepping through the 2D space of hits. Several factors  
435 determine whether a hit is added to the trajectory, including but not limited to

- 436     1. the goodness of the fit of the single hit,  
437     2. the charge of the hit compared to the average charge and RMS of the hits  
438         already forming the trajectory,  
439     3. the goodness of trajectory fit with and without the hit addition,  
440     4. the angle between the two lines formed by the collection of hits before and after  
441         the considered hit in the trajectory.

442 The final product of this reconstruction stage is the collection of bidimensional clusters  
443 on each wire plane, see Figure 6 panel d).

444 **3D Tracking.** The 3D tracking set of algorithms uses clusters close in time on  
445 the induction and collection planes as starting point to form a 3D track. Firstly, it  
446 construct a tentative 3D trajectory using the edges of the clusters. Then, it projected  
447 back the tentative trajectory on to the planes and adjusts the parameters of the 3D

448 track fit such that they minimize the distance between the fit projections and the  
449 track hits in all wire planes simultaneously. Tridimensional tracking can use multiple  
450 clusters in one plane, but it can never break them in smaller groups of hits. This  
451 algorithm was first developed for the ICARUS collaboration [13]. The final product  
452 of this reconstruction stage is the formation of tridimensional objects in the TPC  
453 active volume, see Figure 6 panel e).

454

455 **Calorimetry.** The last step in the event reconstruction chain is to assign calorimetric  
456 information to the track (or shower) objects. Calorimetry is performed separately  
457 on the different planes. A multi-step procedure is needed to retrieve the energy  
458 deposited in the TPC from the charge seen by the wires. For each hit associated with  
459 the track object, the calorimetry algorithms calculate the charge seen on every wire  
460 using the area underneath the gaussian fit; then, they correct this raw charge by the  
461 electron life time, the electronic noise on the considered wire and the recombination  
462 effect. Lastly an overall calibration of the energy, explained in detail in section 2.4.1,  
463 is applied and the calorimetric information for the given track is assigned. Even if  
464 calorimetry is done in 2D, it benefits from the 3D tracking information; typical information  
465 available after the calorimetric reconstruction are the total energy deposited  
466 by the particle and its stopping power  $dE/dx$  at each “track pitch”, i.e. at each 2D  
467 projection on the wire plane of the 3D trajectory.

## 468 0.2 The Intensity Frontier Program

### 469 0.2.1 Prospects for LArTPCs in Neutrino Physics: SBN and 470 DUNE

471 The ArgoNeut experiment [12] initiated the US LArTPC neutrino program. Following  
472 the success of this small TPC on the NuMI beam, a wide program of LArTPCs

473 on neutrino beams has flourished. The construction of LArTPCs as near and far  
474 detectors at different baseline allows for the exploration of some of the fundamental  
475 questions in neutrino physics today illustrated in section ??.

476 The Short-Baseline Neutrino (SBN) [14] program at Fermilab is tasked with con-  
477 clusively assess the nature of the “LSND and MiniBooNE anomalies” [9, 10, 15], re-  
478 solving the mystery of sterile neutrinos at the eV<sup>2</sup> scale. The SBN program entails  
479 three surface LArTPCs positioned on the Booster Neutrino Beam at different dis-  
480 tances from the neutrino production in oder to fully exploit the L/E dependence of  
481 the oscillation pattern: SBND (100 m from the decay pipe), MicroBooNE (450 m),  
482 and ICARUS (600 m). Within the oscillation context, the choice of the LArTPC tech-  
483 nology for the SBN detectors changes the set of systematics with respect to LSND  
484 and MiniBooNE, whose detection techniques were both based on Cherenkov light.  
485 In particular, LArTPCs provide excellent electron/photon separation [5] lacking in  
486 Cherenkov detectors which can be leveraged to abate the photon background from  
487 neutral current interactions in  $\nu_e$  searches. MicroBooNE [4], the first detector of  
488 the SBN program to be fully operational, started its first neutrino run in October  
489 2015. MicroBooNE is a 89 ton active volume LArTPC, single drift chamber with  
490 TPC dimensions of 2.6 m (drift) x 2.3 m (heigh) x 10.4 m (depth). MicroBooNE is  
491 positioned at a very similar L/E on the Booster neutrino beam as MiniBooNE has  
492 the scope to directly cross check the MiniBooNE oscillation measurement. In case  
493 MicroBooNE confirms the presence of the “low energy excess” anomaly, SBND and  
494 ICARUS will provide the full measurement of the oscillation parameters. SBND and  
495 ICARUS are both dual drift chambers, whose active volume is respectively 112 ton  
496 and 600 ton. ICARUS is scheduled to become operational by the end of 2018 and  
497 SBND shortly after. Besides the oscillation analysis, the second main goals of SBN is  
498 to perform an extensive campaign of neutrino cross section measurements in argon.  
499 Given the importance of nuclear effects in (relatively) heavy materials, as discussed in

500 section ??, both the oscillation analysis of the SBN program and the measurements  
501 of neutrino properties in DUNE will benefit from such a campaign.

502 On a different neutrino beam and baseline, the DUNE experiment, née LBNE [7],  
503 is the flagship experiment on the medium-long term of US-based neutrino physics,  
504 scheduled to start data taking in 2026. Shooting neutrinos from Fermilab for 800 miles  
505 to the SURF laboratory in South Dakota, DUNE is tasked with performing conclusive  
506 measurements of CP violation in the lepton sector, the neutrino mass ordering and  
507 the  $\theta_{23}$  octant. The DUNE far detector will count four 10 kton LArTPCs, roughly of  
508 dimensions of 19 m (horizontally) x 18 m (vertically) x 66 m (depth).

### 509 0.2.2 Prospects for LArTPCs in GUT Physics: DUNE

510 The experimental exploration of a manifestation of Grand Unified Theory is possible  
511 in DUNE thanks to its sheer mass. In particular, proton decay searches are a capital  
512 topic of DUNE’s wide non-accelerator physics program. The key elements for a  
513 rare decay experiment are: massive active volume, long exposure, high identification  
514 efficiency and low background. Figure 7 shows the current best experimental limits  
515 on nucleon decay lifetime over branching ratio (dots). Historically, the dominant  
516 technology used in these searches has been water Cherenkov detectors: all the best  
517 experimental limits on every decay mode are indeed set by Super-Kamiokande [?, ?].  
518 As shown in section ??, different family of GUTs predict the proton to decay in  
519 different modes. In particular, SUSY flavored GUTs prefer the presence of kaons  
520 in the decay products, e.g.  $p \rightarrow K^+ \bar{\nu}$ . It is particularly important to notice that  
521 the kaon energy for the proton decay mode  $p \rightarrow K^+ \bar{\nu}$  is under Cherenkov threshold  
522 in water. Thus, Super-Kamiokande set the limit on the lifetime for the  $p \rightarrow K^+ \bar{\nu}$   
523 mode by relying on photons from nuclear de-excitation and on the muon tagging in  
524 the kaon decay leptonic mode. For this reason, an attractive alternative approach to  
525 identifying nucleon decay is the use of a LArTPCs, where the kaon is directly visible

526 in the detector. According to [7], DUNE will have an active volume large enough,  
 527 have sufficient shielding from the surface, and will run for lengths of time sufficient  
 528 to compete with Hyper-K, opening up the opportunity for the discovery of nucleon  
 529 decay.

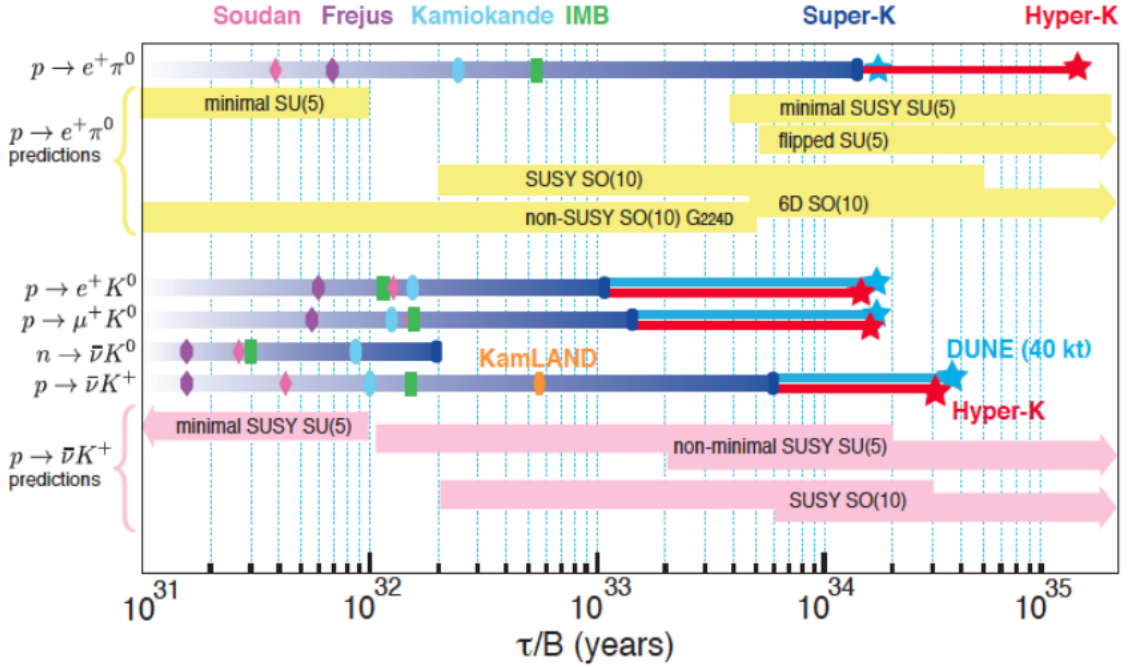


Figure 7: Proton decay lifetime limits from passed and future experiments.

### 530 0.2.3 Enabling the next generation of discoveries: LArIAT

531 LArIAT, a small LArTPC in a test beam, is designed to perform an extensive physics  
 532 campaign centered on charged particle cross section measurements while characteriz-  
 533 ing the detector performance for future LArTPCs. Since LArTPCs represent the most  
 534 advanced experiments for physics at the Intensity Frontier, their complex technology  
 535 needs a thorough calibration and dedicated measurements of some key quantities to  
 536 achieve the precision required for the next generation of discoveries. LArIAT’s goal  
 537 is to provide such calibration and dedicated measurements. The LArIAT LArTPC is  
 538 deployed in a dedicated calibration test beamline at Fermilab. We use the LArIAT

beamline to characterize the charge particles before they enter the TPC: the particle type and initial momentum is known from beamline information. The precise calorimetric energy reconstruction of the LArTPC technology enables the measurement of the total differential cross section for tagged hadrons. The Pion-Nucleus and Kaon-Nucleus total hadronic interaction cross section have never been measured before in argon and they are a fundamental step to shed light on light meson interaction in nuclei per se, while providing a key input to neutrino physics and proton decay studies in future LArTPC experiments like SBN and DUNE.

In order to showcase LArIAT’s utility to SBN and DUNE, we illustrate briefly two comparisons as examples: one regarding neutrino interactions and the second regarding proton decay studies.

The left side of figure 8 shows the distribution of products in momentum spectrum and particle type as simulated in a  $\nu_e$  CC interaction in DUNE (according to [37]); the range of these distribution is to compare with the momentum distribution of light particles in the LArIAT beamline – shown on the right side of figure 8. The momentum spectrum in the LArIAT beamline for electrons, muons and pions – the most abundant particles produced in a  $\nu_e$  CC interaction – covers a wide range of the expected momentum distribution in a neutrino event.

The signature of a proton decay event in the “LAr golden mode” is the presence of a single kaon of about 400 MeV in the detector; the momentum spectrum of the kaon pre and post FSI in such an event as simulated by GENIE is shown on the left side of figure 9. The right side of figure 9 shows the momentum spectrum of kaons in the LArIAT beamline. Kaons arriving to the LArIAT TPC are ideal for proton decay studies, since their momentum in the beamline is just above the typical momentum for kaons in a proton decay event: the majority of LArIAT kaons slow down in the TPC enough to enter the desired momentum window.

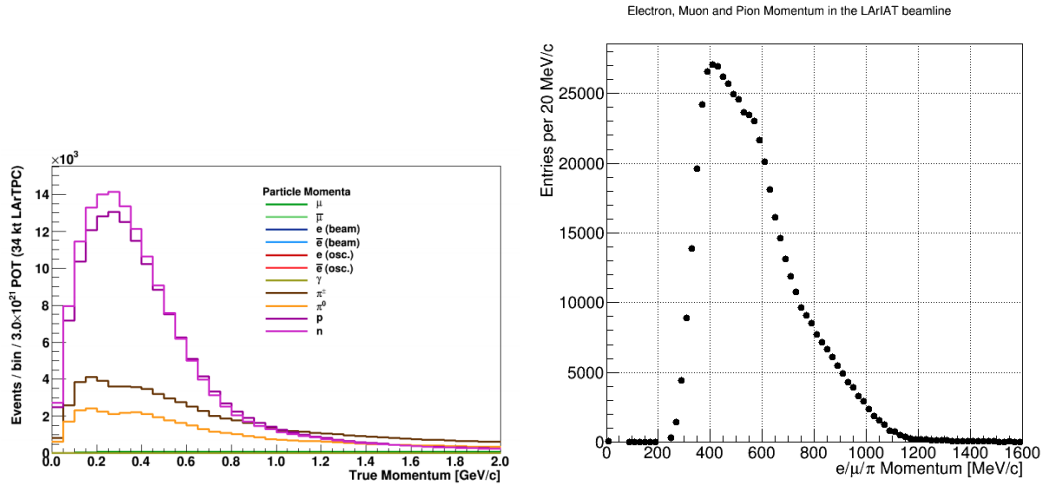


Figure 8: *Left.* Simulation of the products of a  $\nu_e$  CC interaction in DUNE, both in particles type and momentum.  
*Right.* Momentum spectrum for low mass particles ( $e, \mu, \pi$ ) in the LArIAT beamline, negative tune, Run II, Picky Tracks see section ??.

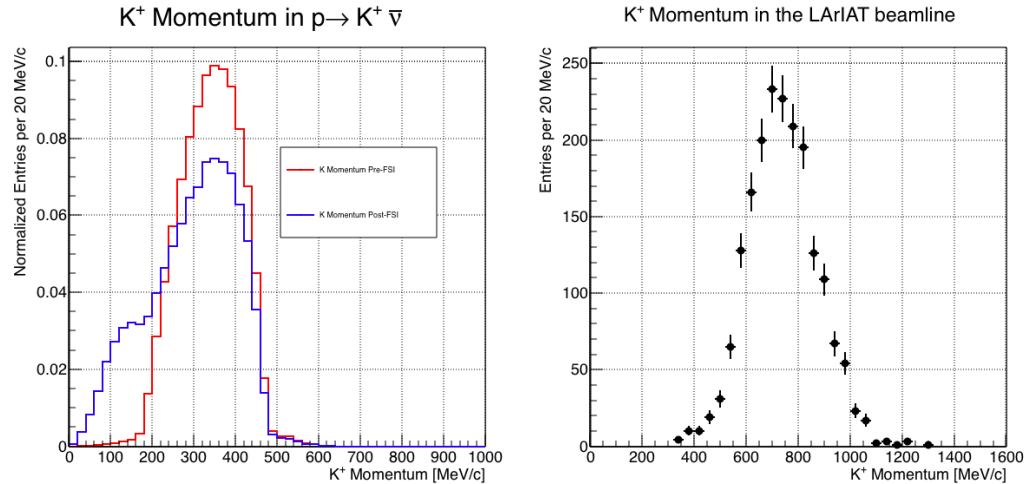


Figure 9: *Left.* Momentum of the kaon outgoing a proton decay  $p \rightarrow K^+ \bar{\nu}$  event as simulated by the Genie 2.8.10 event generator in argon. The red line represents the kaon momentum distribution before undergoing the simulated final state interaction inside the argon nucleus, while the blue line represents the momentum distribution after FSI.  
*Right.* Positive Kaon momentum spectrum in the LArIAT beamline, positive tune, Run II, Picky Tracks see section ??.

565 **Chapter 1**

566 **Total Hadronic Cross Section**

567 **Measurement Methodology**

568 This chapter describes the general procedure employed to measure a total hadronic  
569 differential cross section in LArIAT. Albeit with small differences, both the ( $\pi^-$ ,Ar)  
570 and ( $K^+$ ,Ar) total hadronic cross section measurements rely on the same procedure  
571 described in details in the following sections. We start by selecting the particle of  
572 interest using a combination of beamline detectors and TPC information (Section  
573 ??). We then perform a handshake between the beamline information and the TPC  
574 tracking to assure the selection of the right TPC track (Section 1.2). Finally, we apply  
575 the “thin slice” method and measure the “raw” hadronic cross section (Section 1.3).  
576 A series of corrections are then evaluated to obtain the “true” cross section (Section  
577 1.3.3).

578 At the end of this chapter, we show a sanity check of the methodology against  
579 MC truth information (Section 1.4).

580 **1.1 Event Selection**

581 The measurement of the ( $\pi^-$ ,Ar) and ( $K^+$ ,Ar) total hadronic cross section in LArIAT  
582 starts by selecting the pool of pion or kaon candidates and measuring their momen-  
583 tum. This is done through the series of selections on beamline and TPC information  
584 described in the next sections. The summary of the event selection in data is reported  
585 in Table 1.1.

586 **1.1.1 Selection of Beamline Events**

587 As shown in equation 1.5, we leverage the beamline particle identification and mo-  
588 mentum measurement before entering the TPC as input to evaluate the kinetic  
589 energy for the hadrons used in the cross sections measurements. Thus, we select the  
590 LArIAT data to keep only events whose wire chamber and time of flight information  
591 is registered (line 2 in Table 1.1). Additionally, we perform a check of the plausi-  
592 bility of the trajectory inside the beamline detectors: given the position of the hits  
593 in the four wire chambers, we make sure the particle's trajectory does not cross any  
594 impenetrable material such as the collimator and the magnets steel (line 3 in Table  
595 1.1).

	Run-II Negative Polarity	Run-II Positive Polarity
Events Reconstructed in Beamline	158396	260810
Events with Plausible Trajectory	147468	240954
Beamline $\pi^-/\mu^-/e^-$ Candidate	138481	N.A.
Beamline $K^+$ Candidate	N.A	2837
Events Surviving Pile Up Filter	108929	2389
Events with WC2TPC Match	41757	1081
Events Surviving Shower Filter	40841	N.A.
Available Events For Cross Section	40841	1081

Table 1.1: Number of data events for Run-II Negative and Positive polarity

596    **1.1.2 Particle Identification in the Beamline**

597    In data, the main tool to establish the identity of the hadron of interest is the LArIAT  
598    tertiary beamline, in its function of mass spectrometer. We combine the measurement  
599    of the time of flight,  $TOF$ , and the beamline momentum,  $p_{Beam}$ , to reconstruct the  
600    invariant mass of the particles in the beamline,  $m_{Beam}$ , as follows

$$m_{Beam} = \frac{p_{Beam}}{c} \sqrt{\left(\frac{TOF * c}{l}\right)^2 - 1}, \quad (1.1)$$

601    where  $c$  is the speed of light and  $l$  is the length of the particle's trajectory between  
602    the time of flight paddles.

603    Figure 1.1 shows the mass distribution for the Run II negative polarity runs on  
604    the left and positive polarity runs on the right. We perform the classification of events  
605    into the different samples as follows:

- 606       •  $\pi/\mu/e$ : mass < 350 MeV  
607       • kaon: 350 MeV < mass < 650 MeV  
608       • proton: 650 MeV < mass < 3000 MeV.

609    Lines 4 and 5 in Table 1.1 show the number of negative  $\pi/\mu/e$  and positive  $K$   
610    candidates which pass the mass selection for LArIAT Run-II data.

611    **1.1.3 TPC Selection: Halo Mitigation**

612    The secondary beam impinging on LArIAT secondary target produces a plethora of  
613    particles which propagates downstream. The presence of upstream and downstream  
614    collimators greatly abates the number of particles tracing down the LArIAT tertiary  
615    beamline. However, it is possible that more than one particle sneaks into the LArTPC  
616    during its readout time: the TPC readout is triggered by the particle firing the

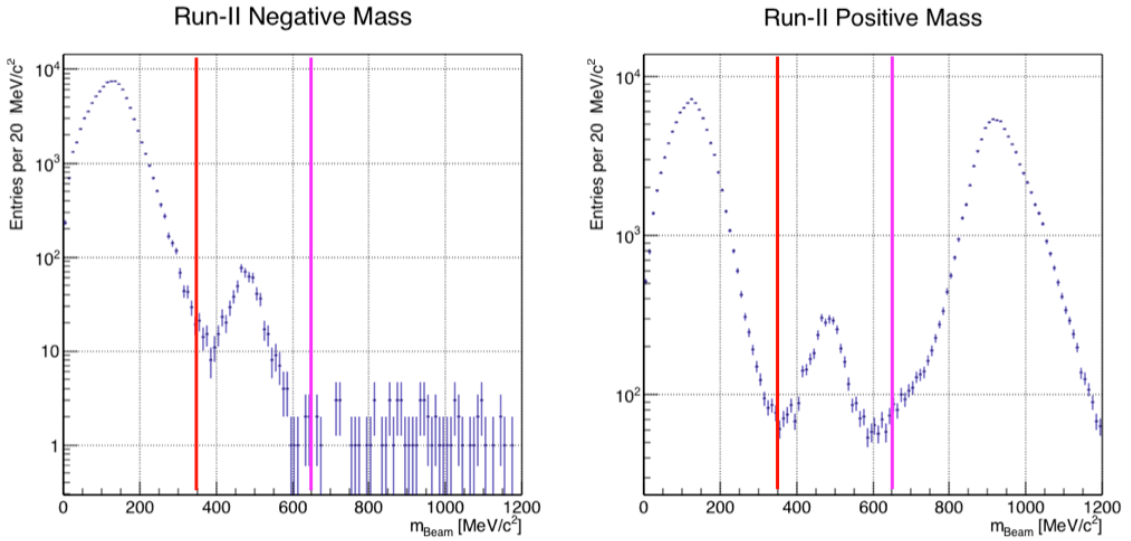


Figure 1.1: Distribution of the beamline mass as calculated according to equation 1.1 for the Run-II events reconstructed in the beamline, negative polarity runs on the left and positive polarity runs on the right. The classification of the events into  $\pi^\pm/\mu^\pm/e^\pm$ ,  $K^\pm$ , or (anti)proton is based on these distributions, whose selection cut are represented by the vertical colored lines.

beamline detectors, but particles from the beam halo might be present in the TPC at the same time. We call “pile up” the additional traces in the TPC. We adjusted the primary beam intensity between LArIAT Run I and Run II to reduce the presence of events with high pile up particles in the data sample. For the cross section analyses, we remove events with more than 4 tracks in the first 14 cm upstream portion of the TPC from the sample (line 6 in Table 1.1).

#### 1.1.4 TPC Selection: Shower Removal

In the case of the  $(\pi^-, \text{Ar})$  cross section, the resolution of beamline mass spectrometer is not sufficient to select a beam of pure pions. In fact, muons and electrons survive the selection on the beamline mass. It is important to notice that the composition of the negative polarity beam is mostly pions, as will be discussed in section 2.2.1. Anyhow, we devise a selection on the TPC information to mitigate the presence of

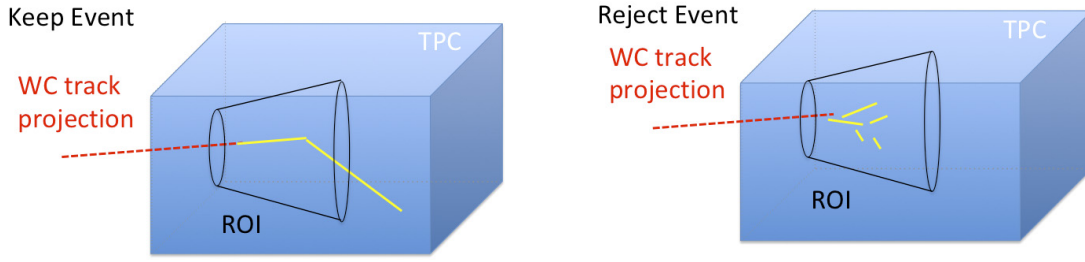


Figure 1.2: Visual rendering of the shower filter. The ROI is a cut cone, with a small radius of 4 cm, a big radius of 10 cm and an height of 42 cm (corresponding to 3 radiation lengths for electrons in Argon).

629 electrons in the sample used for the pion cross section. The selection relies on the  
 630 different topologies of a pion and an electron event in the argon: while the former  
 631 will trace a track inside the TPC active volume, the latter will tend to “shower”, i.e.  
 632 interact with the medium, producing bremsstrahlung photons which pair convert into  
 633 several short tracks. In order to remove the shower topology, we create a region of  
 634 interest (ROI) around the TPC track corresponding to the beamline particle (more  
 635 details on this in the next section). We look for short tracks contained in the ROI, as  
 636 depicted in figure 1.4: if more than 5 tracks shorter than 10 cm are in the ROI, we  
 637 reject the event. Line 8 in Table 1.1) shows the number of events surviving this  
 638 selection.

## 639 1.2 Beamlne and TPC Handshake: the Wire Cham- 640 ber to TPC Match

641 For each event passing the selection on its beamline information, we need to identify  
 642 the track inside the TPC corresponding to the particle which triggered the beamline  
 643 detectors, a procedure we refer to as “WC to TPC match” (WC2TPC for short).  
 644 In general, the TPC tracking algorithm will reconstruct more than one track in the  
 645 event, partially due to the fact that hadrons interact in the chamber and partially

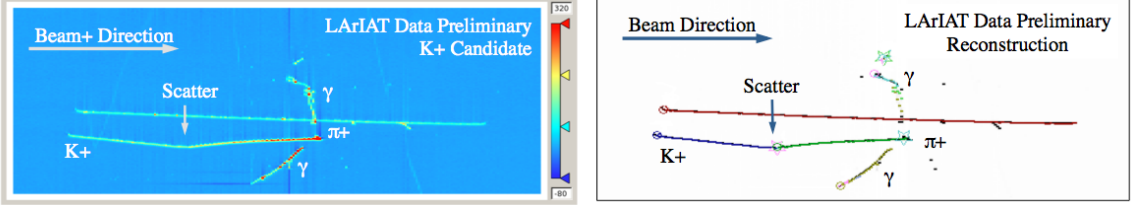


Figure 1.3: Kaon candidate event: on the right, event display showing raw quantities; on the left, event display showing reconstructed tracks. In the reconstructed event display, different colors represent different track objects. A kink is visible in the kaon ionization, signature of a hadronic interaction: the tracking correctly stops at the kink position and two tracks are formed. An additional pile-up track is so present in the event (top track).

646 because of pile up particles during the triggered TPC readout time, as shown in  
 647 figure 1.3.

648 We attempt to uniquely match one wire chamber track to one and only one re-  
 649 constructed TPC track. In order to determine if the presence of a match, we apply  
 650 a geometrical selection on the relative the position of the wire chamber and TPC  
 651 tracks. We start by considering only TPC tracks whose first point is in the first 2  
 652 cm upstream portion of the TPC for the match. We project the wire chamber track  
 653 to the TPC front face where we define the coordinates of the projected point as  $x_{FF}$   
 654 and  $y_{FF}$ . For each considered TPC track, we define  $\Delta X$  as the difference between  
 655 the  $x$  position of the most upstream point of the TPC track and  $x_{FF}$ .  $\Delta Y$  is defined  
 656 analogously. We define the radius difference,  $\Delta R$ , as  $\Delta R = \sqrt{\Delta X^2 + \Delta Y^2}$ . We de-  
 657 fine as  $\alpha$  the angle between the incident WC track and the TPC track in the plane  
 658 that contains them. If  $\Delta R < 4$  cm,  $\alpha < 8^\circ$ , a match between WC-track and TPC  
 659 reconstructed track is found. We describe how we determine the value for the radius  
 660 and angular selection in sec 2.3.1. In MC, we mimic the matching between the WC  
 661 and the TPC track by constructing a fake WC track using truth information at wire  
 662 chamber four. We then apply the same WC to TPC matching algorithm as in data.  
 663 We discard events with multiple WC2TPC matches. We use only those TPC tracks  
 664 that are matched to WC tracks in the cross section calculation.

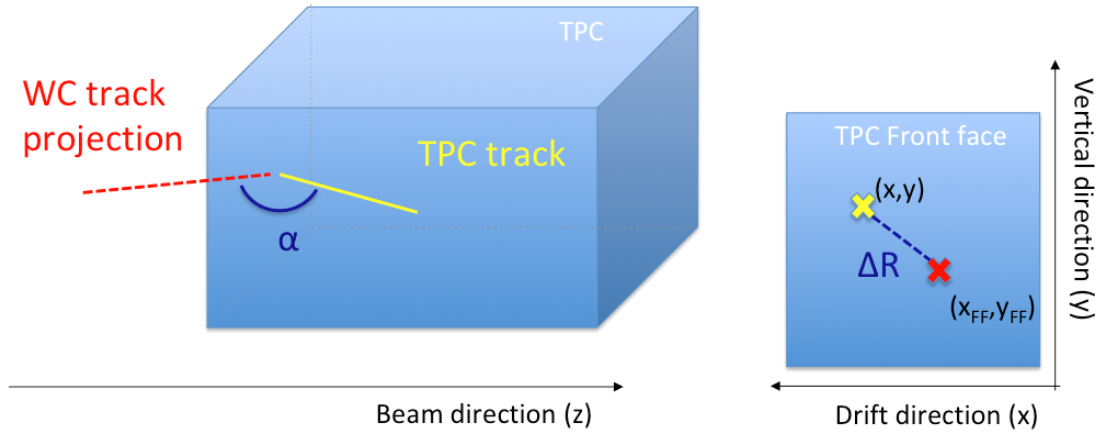


Figure 1.4: Visual rendering of the wire chamber to TPC match.

### 665 1.3 The Thin Slice Method

666 Once we have selected the pool of hadron candidates and we have identified the TPC  
667 track corresponding to the beamline event, we apply the thin slice method to measure  
668 the cross section, as the following sections describe.

#### 669 1.3.1 Cross Sections on Thin Target

670 Cross section measurements on a thin target have been the bread and butter of  
671 nuclear and particle experimentalists since the Geiger-Marsden experiments [29]. At  
672 their core, these types of experiments consist in shooting a beam of particles with a  
673 known flux on a thin target and recording the outgoing flux.

674 In general, the target is not a single particle, but rather a slab of material contain-  
675 ing many diffusion centers. The so-called “thin target” approximation assumes that  
676 the target centers are uniformly distributed in the material and that the target is thin  
677 compared to the projectile interaction length, WC2TPC so that no center of interac-  
678 tion sits in front of another. In this approximation, the ratio between the number of  
679 particles interacting in the target  $N_{Interacting}$  and number of incident particles  $N_{Incident}$   
680 determines the interaction probability  $P_{Interacting}$ , which is the complementary to one

681 of the survival probability  $P_{Survival}$ . Equation 1.2

$$P_{Survival} = 1 - P_{Interacting} = 1 - \frac{N_{Interacting}}{N_{Incident}} = e^{-\sigma_{TOT} n \delta X} \quad (1.2)$$

682 describes the probability for a particle to survive the thin target. This formula relates  
683 the total cross section  $\sigma_{TOT}$ , the density of the target centers  $n$  and the thickness of  
684 the target along the incident hadron direction  $\delta X$ , to the interaction probability<sup>1</sup>.  
685 If the target is thin compared to the interaction length of the process considered,  
686 we can Taylor expand the exponential function in equation 1.2 and find a simple  
687 proportionality relationship between the number of incident and interacting particles,  
688 and the cross section, as shown in equation 1.3:

$$1 - \frac{N_{Interacting}}{N_{Incident}} = 1 - \sigma_{TOT} n \delta X + O(\delta X^2). \quad (1.3)$$

689 Solving for the cross section, we find:

$$\sigma_{TOT} = \frac{1}{n \delta X} \frac{N_{Interacting}}{N_{Incident}}. \quad (1.4)$$

### 690 1.3.2 Not-so-Thin Target: Slicing the Argon

691 The interaction length of pions and kaons in argon is expected to be of the order  
692 of 50 cm for pions and 100 cm for kaons. Thus, the LArIAT TPC, with its 90 cm  
693 of length, is not a thin target. However, the fine-grained tracking of the LArIAT  
694 LArTPC allows us to treat the argon volume as a sequence of many adjacent thin  
695 targets.

696 As described in Chapter ??, LArIAT wire planes consist of 240 wires each. The  
697 wires are oriented at +/- 60° from the vertical direction at 4 mm spacing, while the

---

1. The scattering center density in the target,  $n$ , relates to the argon density  $\rho$ , the Avogadro number  $N_A$  and the argon molar mass  $m_A$  as  $n = \frac{\rho N_A}{m_A}$ .

beam direction is oriented 3 degrees off the  $z$  axis in the  $XZ$  plane. The wires collect  
 signals proportional to the energy loss of the hadron along its path in a  $\delta X = 4$   
 $\text{mm}/\sin(60^\circ) \approx 4.7 \text{ mm}$  slab of liquid argon. Thus, one can think to slice the TPC  
 into many thin targets of  $\delta X = 4.7 \text{ mm}$  thickness along the direction of the incident  
 particle, making a measurement at each wire along the path.

Considering each slice  $j$  a “thin target”, we can apply the cross section calculation  
 from Equation 3.1 iteratively, evaluating the kinetic energy of the hadron as it enters  
 each slice,  $E_j^{kin}$ . For each WC2TPC matched particle, the energy of the hadron  
 entering the TPC is known thanks to the momentum and mass determination by the  
 tertiary beamline,

$$E_{FrontFace}^{kin} = \sqrt{p_{Beam}^2 - m_{Beam}^2} - m_{Beam} - E_{loss}, \quad (1.5)$$

where  $E_{loss}$  is a correction for the energy loss in the dead material between the  
 beamline and the TPC front face. The energy of the hadron at each slab is determined  
 by subtracting the energy released by the particle in the previous slabs. For example,  
 at the  $j^{th}$  point of a track, the kinetic energy will be

$$E_j^{kin} = E_{FrontFace}^{kin} - \sum_{i < j} \Delta E_i, \quad (1.6)$$

where  $\Delta E_i$  is the energy deposited at each argon slice before the  $j^{th}$  point as measured  
 by the calorimetry associated with the tracking.

If the particle enters a slice, it contributes to  $N_{Incident}(E^{kin})$  in the energy bin  
 corresponding to its kinetic energy in that slice. If it interacts in the slice, it then  
 also contributes to  $N_{Interacting}(E^{kin})$  in the appropriate energy bin. The cross section  
 as a function of kinetic energy,  $\sigma_{TOT}(E^{kin})$  will then be proportional to the ratio  
 $\frac{N_{Interacting}(E^{kin})}{N_{Incident}(E^{kin})}$ .

719 **1.3.3 Corrections to the Raw Cross Section**

720 Equation 3.1 is a prescription for measuring the cross section in case of a pure beam  
721 of the hadron of interest and 100% efficiency in the determination of the interaction  
722 point. For example, if LArIAT had a beam of pure pions and were 100% efficient  
723 in determining the interaction point within the TPC, the pion cross section in each  
724 energy bin would be given by

$$\sigma^{\pi^-}(E_i) = \frac{1}{n\delta X} \frac{N_{\text{Interacting}}^{\pi^-}(E_i)}{N_{\text{Incident}}^{\pi^-}(E_i)}. \quad (1.7)$$

725 Unfortunately, this is not the case. In fact, the selection used to isolate pions in the  
726 LArIAT beam allows for the presence of some muons and electrons as background.  
727 Also, the LArIAT TPC is not 100% efficient in determining the interaction point.  
728 Therefore we need to apply two corrections evaluated on the MC in order to extract  
729 the cross section from LArIAT data: the background subtraction and the efficiency  
730 correction. Still using the pion case as example, we estimate the pion cross section in  
731 each energy bin changing Equation 1.7 into

$$\sigma^{\pi^-}(E_i) = \frac{1}{n\delta X} \frac{N_{\text{Interacting}}^{\pi^-}(E_i)}{N_{\text{Incident}}^{\pi^-}(E_i)} = \frac{1}{n\delta X} \frac{\epsilon_i^{\text{inc}}[N_{\text{Interacting}}^{\text{TOT}}(E_i) - B_{\text{Interacting}}(E_i)]}{\epsilon_i^{\text{int}}[N_{\text{Incident}}^{\text{TOT}}(E_i) - B_{\text{Incident}}(E_i)]}, \quad (1.8)$$

732 where  $N_{\text{Interacting}}^{\text{TOT}}(E_i)$  and  $N_{\text{Incident}}^{\text{TOT}}(E_i)$  is the measured content of the interacting  
733 and incident histograms for events that pass the event selection,  $B_{\text{interacting}}(E_i)$  and  
734  $B_{\text{Incident}}(E_i)$  represent the contributions from beamline background, and  $\epsilon_i^{\text{int}}$  and  $\epsilon_i^{\text{inc}}$   
735 are the efficiency corrections for said histograms.

736 As we will show in section ??, the background subtraction for the interacting and  
737 incident histograms can be translated into a corresponding corrections  $C_{\text{Interacting}}^{\pi MC}(E_i)$   
738 and  $C_{\text{Incident}}^{\pi MC}(E_i)$  and the cross section re-written as follows

$$\sigma^{\pi^-}(E_i) = \frac{1}{n\delta X} \frac{\epsilon^{\text{Inc}}(E_i)}{\epsilon^{\text{Int}}(E_i)} \frac{C_{\text{Int}}^{\pi MC}(E_i)}{C_{\text{Inc}}^{\pi MC}(E_i)} \frac{N_{\text{Int}}^{\text{TOT}}(E_i)}{N_{\text{Inc}}^{\text{TOT}}(E_i)}. \quad (1.9)$$

## 739 1.4 Procedure testing with truth quantities

740 The  $(\pi^-, \text{Ar})$  and  $(K^+, \text{Ar})$  total hadronic cross section implemented in Geant4 can be  
741 used as a tool to validate the measurement methodology. We describe here a closure  
742 test done on Monte Carlo to prove that the methodology of slicing the TPC retrieves  
743 the underlying cross section distribution implemented in Geant4 within the statistical  
744 uncertainty.

745 For pions in the considered energy range, the Geant4 inelastic model adopted to  
746 is “BertiniCascade”, while the elastic model “hElasticLHEP”. For kaons, the Geant4  
747 inelastic model adopted to is “BertiniCascade”, while the elastic model “hElasti-  
748 cLHEP”.

749 For the validation test, we fire about a sample of pions and a sample of kaons  
750 inside the LArIAT TPC active volume using the Data Driven Monte Carlo (see section  
751 2.2.2). We apply the thin-sliced method using only true quantities to calculate the  
752 hadron kinetic energy at each slab in order to decouple reconstruction effects from  
753 issues with the methodology. For each slab of 4.7 mm length along the path of the  
754 hadron, we integrate the true energy deposition as given by the Geant4 transportation  
755 model. Then, we recursively subtracted it from the hadron kinetic energy at the TPC  
756 front face to evaluate the kinetic energy at each slab until the true interaction point is  
757 reached. Since the MC is a pure beam of the hadron of interest and truth information  
758 is used to retrieve the interaction point, no correction is applied. Doing so, we obtain  
759 the true interacting and incident distributions for the considered hadron and we obtain  
760 the true MC cross section as a function of the hadron true kinetic energy.

761 Figure 1.5 shows the total hadronic cross section for argon implemented in Geant4

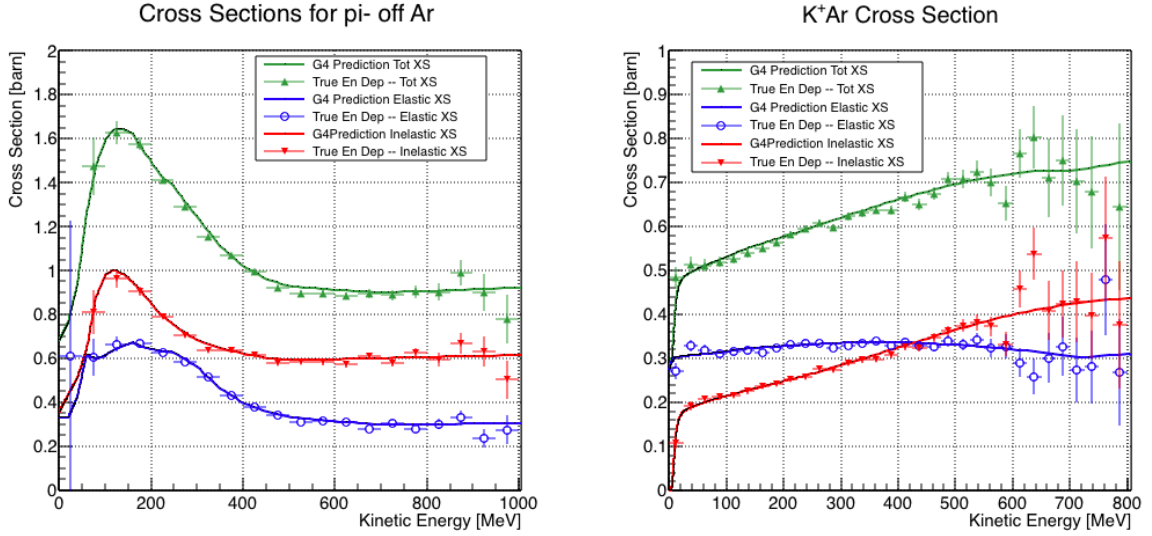


Figure 1.5: Hadronic cross sections for ( $\pi^-$ ,Ar) on the left and ( $K^+$ ,Ar) on the right as implemented in Geant4 10.01.p3 (solid lines) overlaid the true MC cross section as obtained with the sliced TPC method (markers). The total cross section is shown in green, the elastic cross section in blue and the inelastic cross section in red.

762 10.01.p3 (solid lines) overlaid with the true MC cross section as obtained with the  
 763 sliced TPC method (markers) for pions on the left and kaons on the right; the total  
 764 cross section is shown in green, the elastic cross section in blue and the inelastic  
 765 cross section in red. The nice agreement with the Geant4 distribution and the cross  
 766 section obtained with the sliced TPC method gives us confidence in the validity of  
 767 the methodology.

768 **Chapter 2**

769 **Preparatory Work**

770 This chapter describes the preparatory work done on the the data and Monte Carlo  
771 samples used for the cross section analyses. This entails the choice of the data set  
772 and the production of the information needed to construct the Monte Carlo Simula-  
773 tion (section 2.1), the construction and use of said Monte Carlo simulation (section  
774 2.2), the study and optimization of the tracking in the TPC for the cross section  
775 analyses (section 2.3), the calibration of the calorimetry response and related energy  
776 studies (section 2.4).

777 **2.1 Cross Section Analyses Data Set**

778 We choose LArIAT Run-II as the data period for the  $(\pi^-, \text{Ar})$  and  $(K^+, \text{Ar})$  total  
779 hadronic cross section analyses. Data taking for the this period started on 03/15/2016  
780 and ended on 07/31/2016. Since we are interested in beamline and TPC information,  
781 we ask basic requirements on the operational status of the time of fight, wire chambers  
782 and TPC to form the good run list for this period, which we informally call “lovely  
783 runs”.

784 The subset of lovely runs chosen for the  $(\pi^-, \text{Ar})$  total hadronic cross section  
785 analysis includes only the -60A and -100A magnet configurations in negative polarity,

even if LArIAT explored several other beamline configurations during Run-II. The -60A and -100A combined data set accounts for approximately 90% of the total Run-II negative polarity runs. Since the production of beamline Monte Carlo depends on the wanted beamline configuration, the choice of only two beamline settings limits the need for beamline MC production.

Similarly, the subset of lovely runs chosen for the ( $K^+$ ,Ar) total hadronic cross section analysis includes only the +60A and +100A magnet configurations in positive polarity. It should be noted that kaons are extremely rare in the +60A sample, thus the data sample for the ( $K^+$ ,Ar) cross section after the mass selection is about 90% +100A runs, as shown in Table 2.1.

For the first measurements in LArIAT that uses both beamline and TPC information, we choose strict requirements on the reconstruction of the WC tracks, the so-called “Picky Track” sample (see ??). This choice presents two advantages: the uncertainty on the momentum reconstruction for the “Picky Tracks” sample is smaller compared to the “High Yield” sample, and the comparison with the beamline MC results is straightforward. A possible future update and cross check of these analysis would be the use of the High Yield sample, where the statistics is about three times higher.

The breakdown of beamline events as a function of the magnets settings is shown in Table 2.1. The choice of the data sets determines the production of beamline MC and serves as basis for the production of Data Driven MC, as shown in the next sections.

	I = 60 A	I = 100 A	Total
Data Events after $\pi/\mu/e$ Mass Selection	67068	71413	138481
Data Events after $K$ Mass Selection	274	2563	2837

Table 2.1: Number of data events which fit the  $\pi/\mu/e$  or  $K$  mass hypothesis as a function of magnet settings.

808    **2.2 Construction of a Monte Carlo Simulation for**  
809    **LArIAT**

810    For the simulation of LArIAT events and their particle make up, we use a combination  
811    of two MC generators: the G4Beamline Monte Carlo and the Data Driven single  
812    particle Monte Carlo (DDMC). We use the G4Beamline MC to simulate the particle  
813    transportation in the beamline and calculate the particle composition of the beam just  
814    after the fourth Wire Chamber (WC4). In order to simulate the beamline particles  
815    after WC4 and in the TPC, we use the DDMC.

816    **2.2.1 G4Beamline**

817    G4Beamline simulates the beam collision with the LArIAT secondary target, the  
818    energy deposited by the particles in the LArIAT beamline detectors, and the action  
819    of the LArIAT magnets, effectively accounting for particle transportation through the  
820    beam line from the LArIAT target until “Big Disk”, a fictional, void detector located  
821    just before the LArIAT cryostat. At the moment of this writing, G4Beamline does  
822    not simulated the responses of the beam line detectors. It is possible to interrogate  
823    the truth level information of the simulated particles in several points of the geometry.  
824    In order to ease the handshake between G4Beamline and the DDMC, we ask for the  
825    beam composition just after WC4. Since LArIAT data are taken under different  
826    beam conditions, we need to simulate separately the beam composition according to  
827    the magnets’ settings and the secondary beam intensity with G4Beamline. For the  
828    pion cross section analysis the relevant beam conditions are secondary beam energy  
829    of 64 GeV, negative polarity magnet with current of 100 A and 60 A. For the kaon  
830    cross section analysis the relevant beam conditions is a secondary beam energy of 64  
831    GeV, positive polarity magnet with current of 100 A.

	I = -60 A	I = -100 A
G4Pions	68.8 %	87.4 %
G4Muons	4.6 %	3.7 %
G4Electrons	26.6 %	8.9 %

Table 2.2: Simulated beamline composition per magnet settings

### 832 Beam Composition for Negative Pion Cross Section

833 Even if pions are by far the biggest beam component in negative polarity runs, the  
 834 LArIAT tertiary beam is not a pure pion beam. While useful to discriminate between  
 835 pions, kaons, and protons, the beamline detectors are not sensitive enough to discrim-  
 836 inate among the lighter particles in the beam: electrons, muons and pions fall under  
 837 the same mass hypothesis. Thus, we need to assess the contamination from beamline  
 838 particles other than pions in the event selections used for the pion cross section analy-  
 839 sis and correct for its effects. The first step of this process is assessing the percentage  
 840 of electrons and muons in the  $\pi/\mu/e$  beamline candidates via the G4Beamline MC.  
 841 The full treatment of the beamline contamination in the pion cross section calculation  
 842 is described in section ???. Since the beamline composition is a function of the magnet  
 843 settings, we simulate separately events for magnet current of -60A and -100A. Figure  
 844 2.1 shows the momentum predictions from G4Beamline overlaid with data for the  
 845 60A runs (left) and for the 100A runs (right). The predictions for electrons, muons  
 846 and pions have been staggered and their sum is area normalized to data. Albeit not  
 847 perfect, these plots show a reasonable agreement between the momentum shapes in  
 848 data and MC. We attribute the difference in shape to the lack of simulation of the  
 849 WC efficiency in the MC which is momentum dependent and leads to enhance the  
 850 number events in the center of the momentum distribution.

851 Table 2.2 shows the beam composition per magnet setting after the mass selection  
 852 according to the G4Beamline simulation.

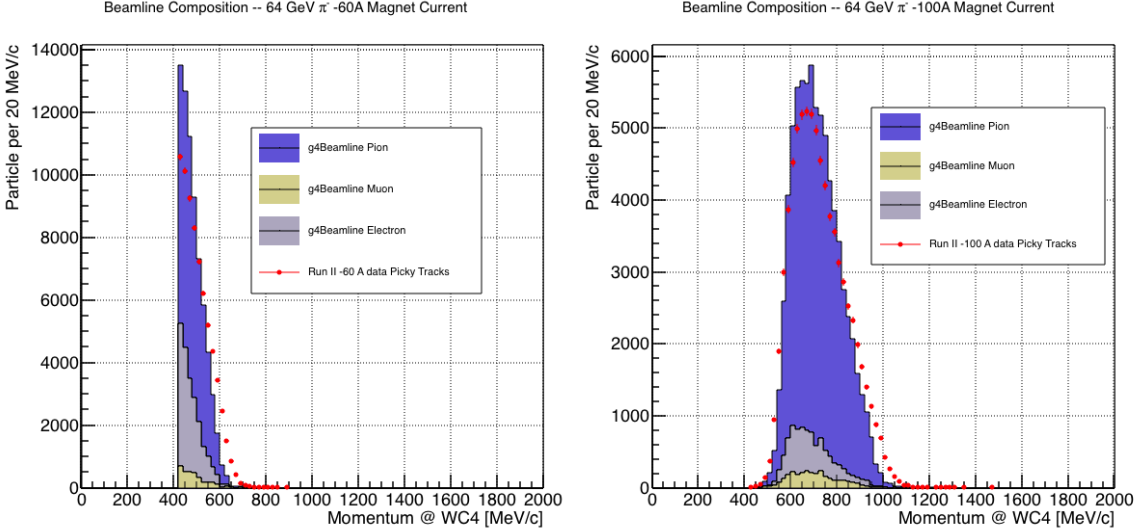


Figure 2.1: Beam composition for the -60A runs (left) and -100A runs (right). The solid blue plot represents the simulated pion content, the yellow plot represents the simulated muon content and the grey plot represents the simulated electron content. The plots are area normalized to the number of data events, shown in red.

### 853 Beam Composition for Positive Kaon Cross Section

854 In the positive polarity runs, the tertiary beam composition is mainly pions and pro-  
 855 tons. The left side of Figure 2.2 shows the predictions for the momentum spectra  
 856 for the 100A positive runs according to G4Beamline (solid colors) overlaid with data  
 857 (black points). Since the LArIAT beamline detectors can discriminate between kaons  
 858 and other particles, we do not rely on the G4Beamline simulation to estimate the  
 859 beamline contamination in the pool of kaon candidates (as in the case of the pion  
 860 cross section), but rather we use a data driven approach. The basic idea of this data  
 861 driven approach is to estimate the bleed over from high and low mass peaks under the  
 862 kaon peak by fitting the tails of the  $\pi/\mu/e$  and proton mass distributions, as shown  
 863 in Figure 2.2 right side. Since the shape of the tails is unknown, the estimate is done  
 864 multiple times varying the range and shape for reasonable functions. For example, to  
 865 estimate the proton content under the kaon peak, we start by fitting the left tail of  
 866 the proton mass distribution with a gaussian function between  $650 \text{ MeV}/c^2$  and  $750$

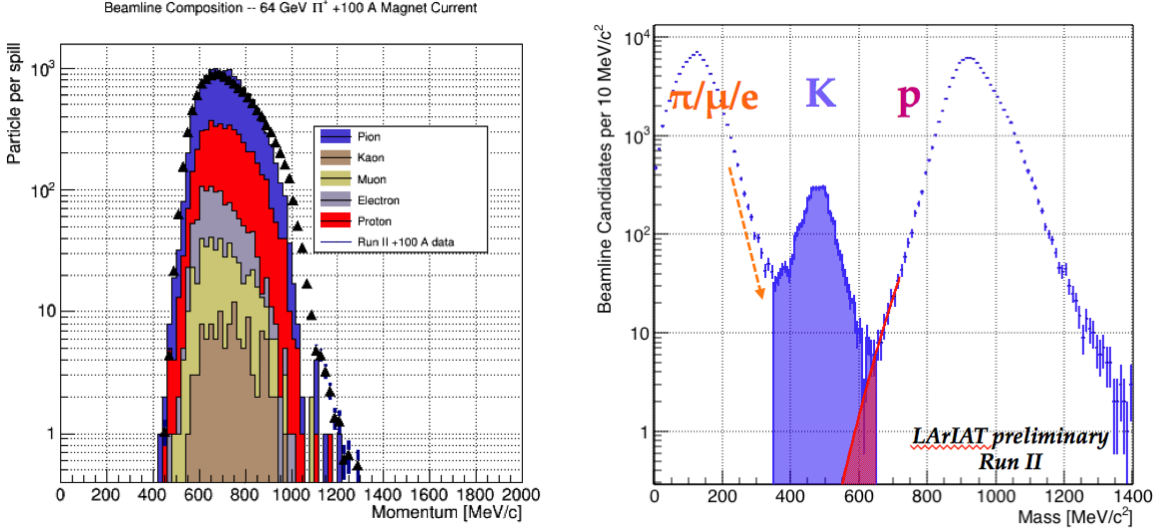


Figure 2.2: *Left.* Beam composition for the +100A runs after WC4 (no mass selection applied). The solid blue plot represents the simulated pion content, the yellow plot represents the simulated muon content and the grey plot represents the simulated positron content, the red the proton content and the mustard the kaon content. The plots are area normalized to the number of data events, shown in black.*Right.* Mass distribution for the Run-II positive runs, where the area under the kaon mass peak is highlighted in purple. The area under the extension of a possible fit for the proton tail is highlighted in red.

867  $MeV/c^2$ . We extend the fit function under the kaon peak and integrate the between  
 868 350-650  $MeV/c^2$ . We integrate the mass histogram in the same range and calculate  
 869 the proton contamination as the ratio between the two integrals. We repeat this pro-  
 870 cedure for several fit shapes (gaussian, linear and exponential functions are used) and  
 871 tail ranges. Finally, we calculate the contamination as the weighted average of single  
 872 estimates, where the weights are calculated to be the  $1./\chi^2$  of the tail fits. The pro-  
 873 cedure is repeated for lighter particles mass peak independently. With 12 iterations  
 874 of this method we find a proton contamination of  $0.2 \pm 0.5 \%$  and a contamination  
 875 from the lighter particles of  $5 \pm 2 \%$ .

876 **2.2.2 Data Driven MC**

877 The Data Driven single particle Monte Carlo (DDMC) is a single particle gun which  
878 simulates the particle transportation from WC4 into the TPC leveraging on the beam-  
879 line data information. The DDMC uses the data momentum and position at WC4  
880 to derive the event generation: a general sketch of the DDMC workflow is shown in  
881 Figure 2.3.

882 When producing a DDMC sample, beam line data from a particular running pe-  
883 riod and/or running condition are selected first. For example, data for the negative  
884 60A runs and for the negative 100A runs inform the event generation stage of two  
885 different DDMC samples. Figure 2.4 schematically shows the data quantities of in-  
886 terest leveraged from data: the momentum ( $P_x, P_y, P_z$ ) and position ( $X, Y$ ) at WC4.  
887 For each data event, we obtain the particle position ( $X, Y$ ) at WC4 directly from the  
888 data measurement; we calculate the components of the momentum using the beamline  
889 measurement of the momentum magnitude in conjunction with the hits on WC3 and  
890 WC4 to determine the direction of the momentum vector, as described in section ???.  
891 The momentum and position of the selected data form a 5-dimensional tuple, which  
892 we sample thousands of times through a 5-dimensional hit-or-miss sampling procedure  
893 to generate the MC events. This produces MC  $P_x, P_y, P_z, X, Y$  distributions with the  
894 same momentum and position distributions as data, with the additional benefit of  
895 accounting for the correlations between the considered variables. As an example, the  
896 results of the DDMC generation compared to data for the kaon +100A sample are  
897 shown in figure 2.5 for the  $P_z$ ,  $X$  and  $Y$  distributions; as expected, MC and data agree  
898 within the statistical uncertainty by construction. A LArSoft simulation module then  
899 launches single particle MC from  $z = -100$  cm (the location of the WC4) using the  
900 MC generated events. The particles are free to decay and interact in their path from  
901 WC4 to the TPC according to the Geant4 simulation.

902 Using the DDMC technique ensures that the MC and data particles have very

903 similar momentum, position and angular distributions at WC4 and allows us to use  
 904 the MC sample in several occasions, for example to calibrate the energy loss upstream  
 905 of the TPC (see Section 2.2.3) or to study the tracking and the calorimetric perfor-  
 906 mance (sections 2.3 and 2.4). A small caveat is in order here: the DDMC is a single  
 907 particle Monte Carlo, which means that the beam pile-up is not simulated.

908 Six samples are the basis fo the MC used in the pion cross section measurement:  
 909 three samples of  $\sim 340000$  pions, muons and electrons to simulate the negative 60A  
 910 runs, and three samples of  $\sim 340000$  pions, muons and electrons for the negative 100A  
 911 runs.

912 The MC used for the kaon cross section analysis is a sample of **NUMBERS** kaons.

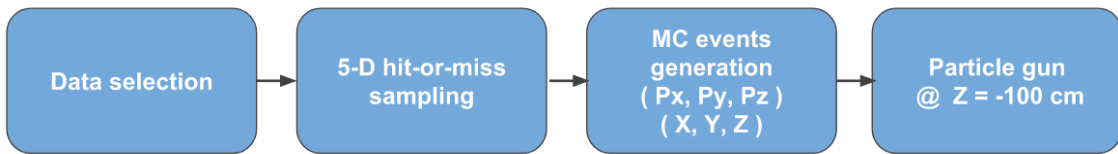


Figure 2.3: Workflow for Data Driven single particle Monte Carlo production.

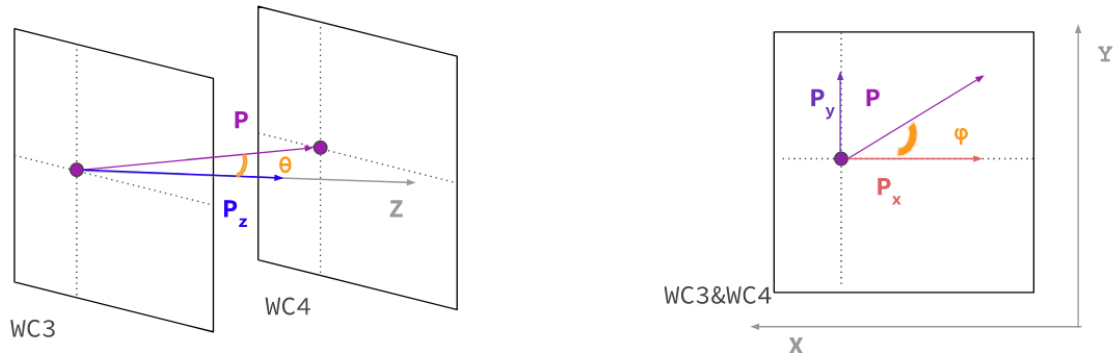


Figure 2.4: Scheme of the quantities of interest for the DDMC event generation:  $P_x, P_y, P_z, X, Y$  at WC4.

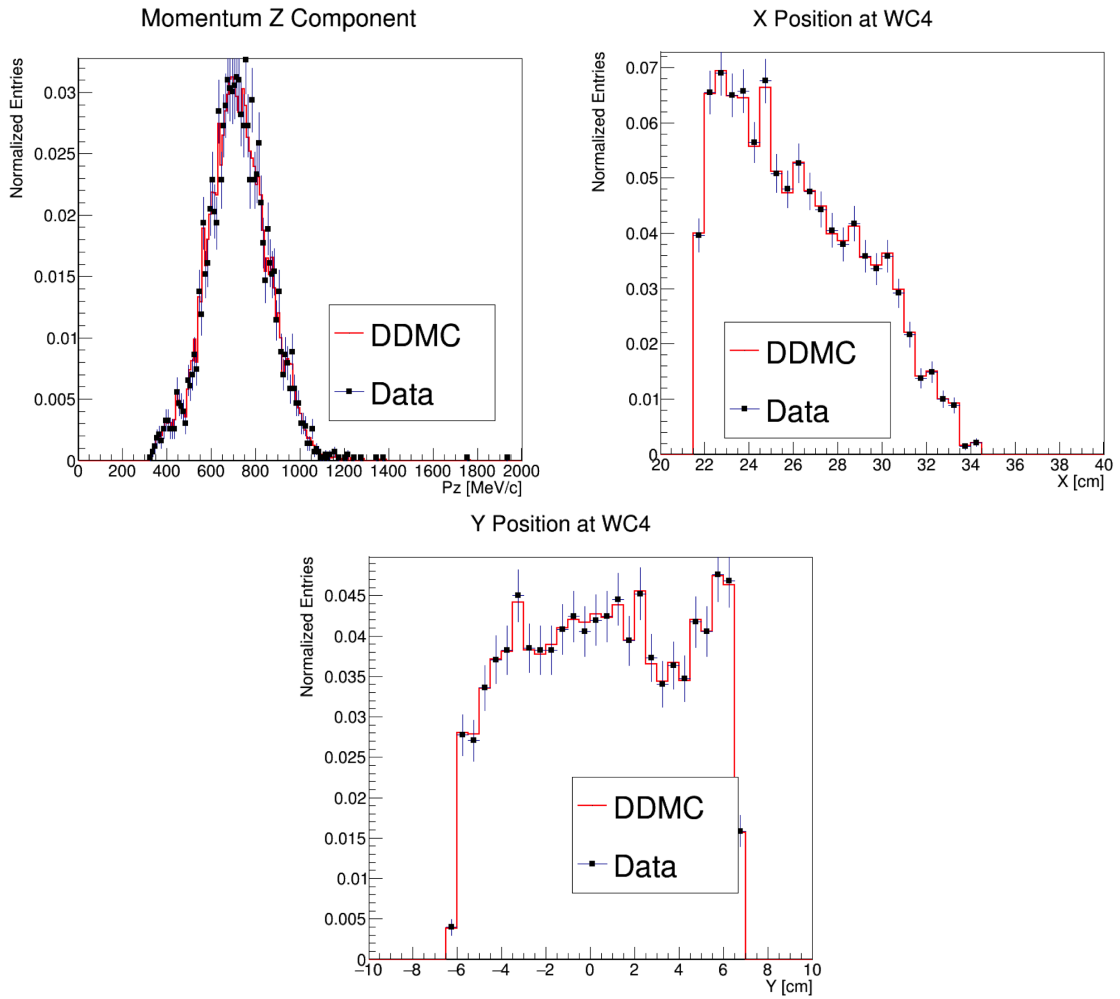


Figure 2.5: Comparison between generated quantities and data distributions for the 100A kaon sample: Z component of the momentum at WC4 (top left), X position at Wire Chamber 4 (top right), Y position at Wire Chamber 4 (bottom).

### 913 2.2.3 Estimate of Energy Loss before the TPC

914 The beamline particles travel a path from where their momentum is measured in  
 915 the beamline until they are tracked again inside the TPC. In the LArIAT geometry,  
 916 a particle leaving the WC4 will encounter the materials listed in Table 2.3 before  
 917 being registered again. The energy lost by the particle in this non-instrumented  
 918 material modifies the particle’s kinetic energy and directly affects the cross section  
 919 measurement, as shown in equation 1.5.

Material	density [g/cm <sup>3</sup> ]	width [cm]
Fiberglass laminate (G10)	1.7	1.28
Liquid Argon	1.4	3.20
Stainless Steel	7.7	0.23
Titanium	4.5	0.04
Air	$1.2 \cdot 10^{-3}$	89.43
Plastic Scintillator	1.03	1.20 (+ 1.30)

Table 2.3: LArIAT material budget from WC4 to the TPC Front Face.

We derive an estimate of the energy loss between the beamline momentum measurement and the TPC ( $E_{loss}$ ) from the pion DDMC sample, since this quantity is not measurable directly on data. The  $E_{loss}$  distribution for the 60A and 100A pion sample is shown in figure 2.6, left and right respectively. A clear double peaked structure is visible, which is due to the particles either missing or hitting the HALO paddle: a schematic rendering of this occurrence is shown in figure 2.7. The kinematic at WC4 determines the trajectory of a particle and whether or not it will hit the halo paddle. In figure 2.8 , we plot the true horizontal component of the momentum  $P_x$  versus the true  $X$  position at WC4 for pions missing the halo paddle (left) and for pions hitting the halo paddle (right) for the 60A MC simulation runs – analogous plots are obtained with the 100A simulation. These distributions can be separated drawing a line in this position-momentum space. We use a logistic regression [8] as a classifier to find the best separating line, shown in both plots as the red line. We classify as

“hitting the halo paddle” all pions whose  $P_x$  and  $X$  are such that

$$P_x + 0.02 * X - 0.4 < 0$$

and as “missing the halo paddle” all pions whose  $P_x$  and  $X$  are such that

$$P_x + 0.02 * X - 0.4 > 0,$$

where the coefficients of the line are empirically found by the logistic regression estimation. Overall, this simple method classifies in the right category (hit or miss) about 86% of the pion events. In MC, we assign  $E_{loss} = 32 \pm 4$  MeV for pion events classified as “hitting the halo paddle”; we assign  $E_{loss} = 24 \pm 3$  MeV for pion events classified as “missing the halo paddle”. We apply the same classifier on data. A scan of the simulated geometry showed an excess of 3 cm of un-instrumented argon compared with the surveyed detector geometry. We account for this difference by assigning in data  $E_{loss} = 24 \pm 6$  MeV for pion events classified as “hitting the halo paddle” and  $E_{loss} = 17 \pm 6$  MeV for pion events classified as “missing the halo paddle”, where the uncertainty is derived as the standard deviation of the double peaked distribution.

The summary of the values for used for  $E_{Loss}$  for the pion sample is listed in table 2.4 with the analogous results for the study on the kaon case.

	$E_{loss}$ [MeV]	
	Hitting Halo	Missing Halo
Pion MC	$32 \pm 4$	$24 \pm 3$
Pion Data	$25 \pm 6$	$17 \pm 6$
Kaon MC	$37 \pm 5$	$31 \pm 4$
Kaon Data	$26 \pm 6$	$22 \pm 6$

Table 2.4: Energy loss for pions and kaons.

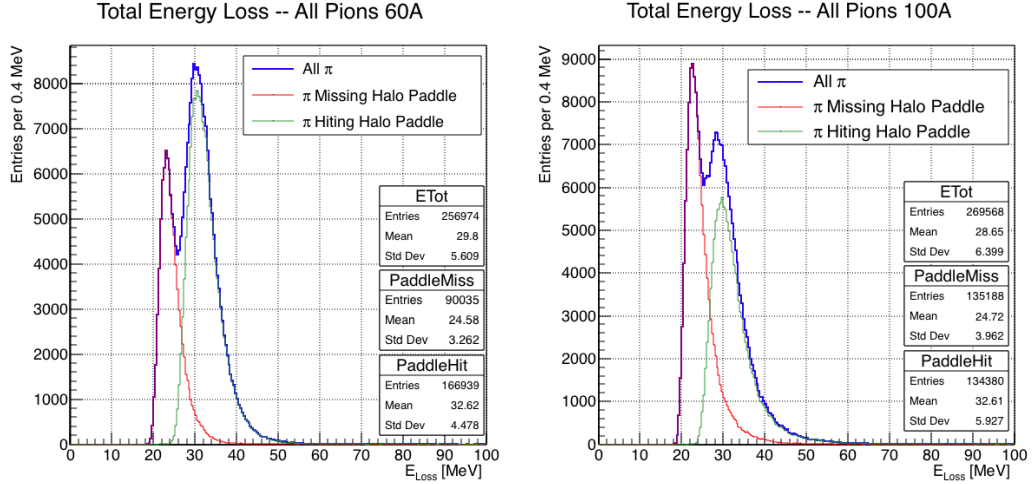


Figure 2.6: True energy loss between WC4 and the TPC front face according to the MC simulation of negative pions of the 60A runs (left) and of the 100A runs (right). The distribution for the whole data sample is shown in blue, the distribution for the pions missing the halo is shown in red, and the distribution for the pions hitting the halo is shown in green.

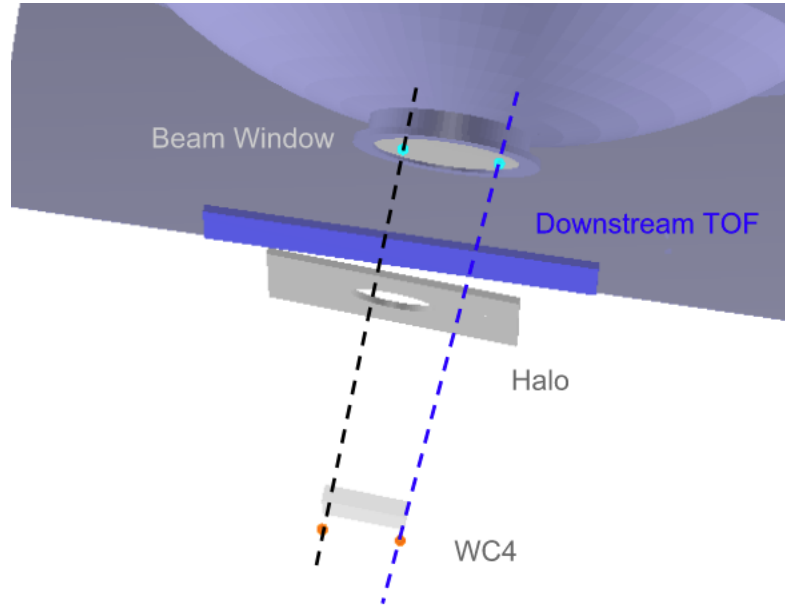


Figure 2.7: Schematic rendering of the particle path between WC4 and the TPC front face. The paddle with the hollow central circle represents the Halo paddle. We illustrate two possible trajectories: in black, a trajectory that miss the paddle and goes through the hole in the Halo, in blue a trajectory that hits the Halo paddle and goes through the scintillation material.

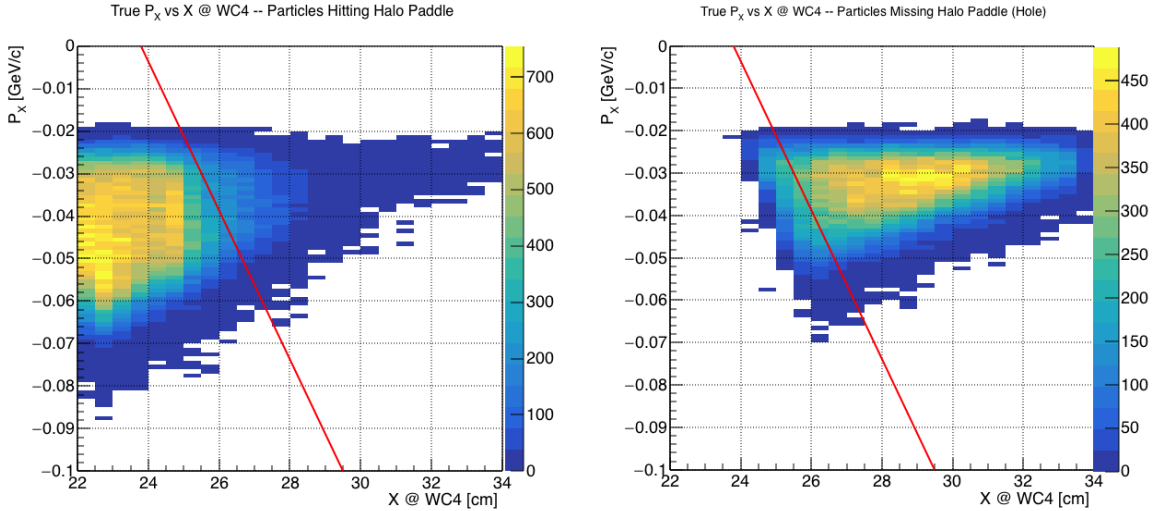


Figure 2.8: Horizontal component of the true momentum vs the horizontal position at WC4 for MC simulated pions of the 60A runs. The plot on the left shows the distribution for pion that miss the halo paddle and the plot on the right shows the distributions for pions that hit the halo. The form of the classifier is overlaid to both plots (red line).

### 933 2.3 Tracking Studies

934 In this section, we describe three studies. The first is a justification of the selection  
 935 criteria for the beamline handshake with the TPC information. We perform this  
 936 study to boost the correct identification of the particles in the TPC associated with  
 937 the beamline information, while maintaining sufficient statistics for the cross section  
 938 measurement. The second study is an optimization of the tracking algorithm, with  
 939 the scope of maximizing the identification of the hadronic interaction point inside the  
 940 TPC. These two studies are related, since the optimization of the tracking is per-  
 941 formed on TPC tracks which have been matched to the wire chamber track; in turn,  
 942 the tracking algorithm for TPC tracks determines the number of reconstructed tracks  
 943 in each event used to try the matching with the wire chamber track. Starting with  
 944 a sensible tracking reconstruction, we perform the WC2TPC matching optimization  
 945 first, then the tracking optimization. The WC2TPC match purity and efficiency are  
 946 then calculated again with the optimized tracking.

947        The third study is an evaluation of the angular resolution of the tracking algorithm  
948        in data and MC, which is particularly important in the context of the cross section  
949        analyses.

950        **2.3.1 Study of WC to TPC Match**

951        Plots I want in this section:

- 952        1. WC2TPC MC DeltaX, DeltaY and  $\alpha$

953        Scope of this study is assessing the goodness of the wire chamber to TPC match  
954        on Monte Carlo and decide the selection values we will use on data. A word of caution  
955        is necessary here. With this study, we want to minimize pathologies associated with  
956        the presence of the primary hadron itself, e.g. the incorrect association between the  
957        beamline hadron and its decay products inside the TPC. Assessing the contamination  
958        from pile-up<sup>1</sup>, albeit related, is beyond the scope of this study.

959        In MC, we are able to define a correct WC2TPC match using the Geant4 truth  
960        information. We are thus able to count how many times the WC tracks is associated  
961        with the wrong TPC reconstructed track.

962        We define a correct match if the all following conditions are met:

- 963        - the length of the true primary Geant4 track in the TPC is greater than 2 cm,  
964        - the length of the reconstructed track length is greater than 2 cm,  
965        - the Z position of the first reconstructed point is within 2 cm from the TPC  
966        front face  
967        - the distance between the reconstructed track and the true entering point is the  
968        minimum compared with all the other reconstructed tracks.

---

1. We remind the reader that the DDMC is a single particle Monte Carlo, where the beam pile up is not simulated.

969        In order to count the wrong matches, we consider all the reconstructed tracks  
 970        whose Z position of the first reconstructed point lies within 2 cm from the TPC front  
 971        face. Events with true length in TPC < 2 cm are included. Since hadrons are shot  
 972        100 cm upstream from the TPC front face, the following two scenarios are possible  
 973        from a truth standpoint:

974        [Ta ] the primary hadron decays or interact strongly before getting to the TPC,

975        [Tb ] the primary hadron enters the TPC.

976        As described in Section 1.2, we define a WC2TPC match according to the relative  
 977        position of the WC and TPC track parametrized with  $\Delta R$  and the angle between  
 978        them, parametrized with  $\alpha$ . Once we choose the selection values  $r_T$  and  $\alpha_T$  to de-  
 979        termine a reconstructed WC2TPC match, the following five scenarios are possible in  
 980        the truth to reconstruction interplay :

981        1) only the correct track is matched

982        2) only one wrong track is matched

983        3) the correct track and one (or more) wrong tracks are matched

984        4) multiple wrong tracks matched.

985        5) no reconstructed tracks are matched

986        Since we keep only events with one and only one match, we discard cases 3), 4)  
 987        and 5) from the events used in the cross section measurement. For each set of  $r_T$  and  
 988         $\alpha_T$  selection value, we define purity and efficiency of the selection as follows:

$$\text{Efficiency} = \frac{\text{Number of events correctly matched}}{\text{Number of events with primary in TPC}}, \quad (2.1)$$

$$\text{Purity} = \frac{\text{Number of events correctly matched}}{\text{Total number of matched events}}. \quad (2.2)$$

989       Figure 2.9 shows the efficiency (left) and purity (right) for WC2TPC match as a  
 990       function of the radius,  $r_T$ , and angle,  $\alpha_T$ , selection value. It is apparent how both  
 991       efficiency and purity are fairly flat as a function of the radius selection value at a  
 992       given angle. This is not surprising. Since we are studying a single particle gun Monte  
 993       Carlo sample, the wrong matches can occur only for mis-tracking of the primary or  
 994       for association with decay products; decay products will tend to be produced at large  
 995       angles compared to the primary, but could be fairly close to the in  $x$  and  $y$  projection  
 996       of the primary. The radius cut would play a key role in removing pile up events.

997       For LArIAT cross section measurements, we generally prefer purity over efficiency,  
 998       since a sample of particles of a pure species will lead to a better measurement. Ob-  
 999       viously, purity should be balanced with a sensible efficiency to avoid rejecting the  
 1000      whole sample.

1001       We choose  $(\alpha_T, r_T) = (8 \text{ deg}, 4 \text{ cm})$  and get a MC 85% efficiency and 98% purity  
 1002       for the kaon sample and a MC 95% efficiency and 90% purity for the pion sample.

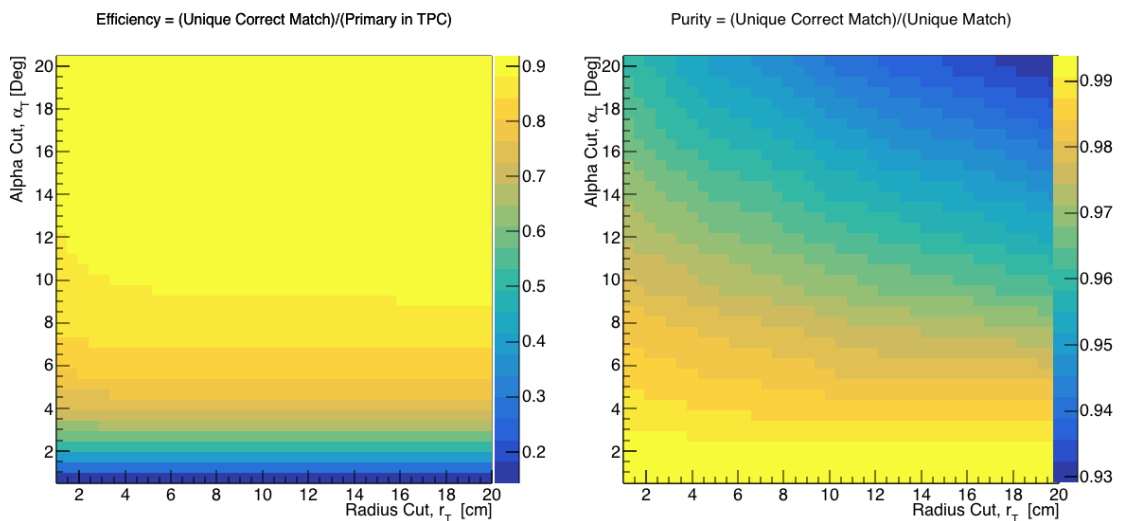


Figure 2.9: Efficiency (left) and purity (right) for WC2TPC match as a function of the radius and angle selections for the kaon sample.

1003 **2.3.2 Tracking Optimization**

1004 **2.3.3 Angular Resolution**

1005 Scope of this study is to understand and compare the tracking performances and  
1006 angular resolution of the TPC tracking on data and MC. We use the angular resolution  
1007 of the tracking to determine the value of smallest angle that we can reconstruct with  
1008 a non-zero efficiency, effectively determining a selection on the angular distribution  
1009 of the cross section measurement due to the tracking performance. This study is  
1010 performed on the pion sample, but its results are extrapolated to the kaon case.

1011 We start by selecting all the WC2TPC matched tracks used for the cross section  
1012 analysis. These tracks can contain from a minimum of 3 3D-space points to a maxi-  
1013 mum of 240 3D-space points. We fit a line to all the 3D-space points associated with  
1014 the track. For each track we calculate the average distance between each point in  
1015 space and the fit line as follows

$$\bar{d} = \frac{\sum_i^N d_i}{N}, \quad (2.3)$$

1016 where  $N$  is the number of 3D-space points of the track and  $d_i$  is the distance of the  
1017  $i$ -th space point to the line fit. Several tests to compare the goodness of fit between  
1018 data and MC have been considered. We decided to use  $\bar{d}$  for its straightforward  
1019 interpretation. The  $\bar{d}$  distribution for data and MC is shown in Figure 2.10 and  
1020 shows a relatively good agreement between data and MC.

1021 A visual representation of the procedure used to evaluate the angular resolution is  
1022 shown in Figure 2.12. For each track, we order the space points according to their Z  
1023 position along the positive beam direction (panel a) and we split them in two sets: the  
1024 first set contains all the points belonging to the first half of the track and the second  
1025 set contains all the points belonging the second half of the track. We remove the last  
1026 four points in the first set and the first four points in the second set, so to have a  
1027 gap in the middle of the original track (panel b). We fit the first and the second set

1028 of points with two lines (panel c). We then calculate the angle between the fit of the  
 1029 first and second half  $\alpha$  (panel d). The angle  $\alpha$  determines the spatial resolution of  
 1030 the tracking. The distributions for data and MC for  $\alpha$  are given in Figure 2.11. The  
 1031 mean of the data and MC angular resolution are respectively

$$\bar{\alpha}_{Data} = (5.0 \pm 4.5) \text{ deg}, \quad (2.4)$$

$$\bar{\alpha}_{MC} = (4.5 \pm 3.9) \text{ deg}. \quad (2.5)$$

1032 Interaction angles smaller than the angle resolution are indistinguishable for the  
 1033 reconstruction. Therefore, we assess our ability to measure the cross section to be  
 1034 limited to interaction angles greater than 5.0 deg. More accurate studies of the angular  
 1035 resolution as a function of the kinetic energy and track length, albeit interesting, are  
 1036 left for an improvement of the analysis.

1037 It is beneficial to take a moment to describe the definition of interaction angle.  
 1038 In case of elastic scattering, the definition is straightforward: the interaction angle is  
 1039 the angle between the incoming and outgoing pion, i.e.

$$\theta = \cos^{-1} \left( \frac{\vec{p}_{\text{incoming}} \cdot \vec{p}_{\text{outgoing}}}{|\vec{p}_{\text{incoming}}| |\vec{p}_{\text{outgoing}}|} \right). \quad (2.6)$$

1040 In case of inelastic scattering, the presence of several topologies requires a more  
 1041 complex definition, as shown in figure 2.13. We define the scattering angle as the  
 1042 biggest of the angles between the incoming pion and the visible daughters, where the  
 1043 visible daughters are charged particles that travel more than 0.47 cm in the detector  
 1044 (see panel a); in case all the daughters are invisible, the angle is assigned to be 90  
 1045 deg (see panel b). We chose this working definition of scattering angle for inelastic  
 1046 scattering keeping in mind how our tracking reconstruction works: the tracking will  
 1047 stop correctly in case of all the daughters are not visible in the detector and it is

1048 likely to stop correctly if multiple daughters form an interaction vertex. The only  
 1049 “dangerous” case is the production of one charged daughter plus neutrals, which we  
 1050 can study with this working definition of scattering angle (see panel c).

1051 We can see the effects of the angular resolution on the cross section by plotting the  
 1052 true Geant4 cross section for interaction angles greater than a minimum interaction  
 1053 angle. Figure 2.14 shows the true Geant4 cross section for interaction angles greater  
 1054 than 0 deg (green), 4.5 deg (red), 5.0 deg (blue) and 9.0 deg (yellow). A small 0.5 deg  
 1055 systematic shift between the mean of the data and MC angular resolution is present.

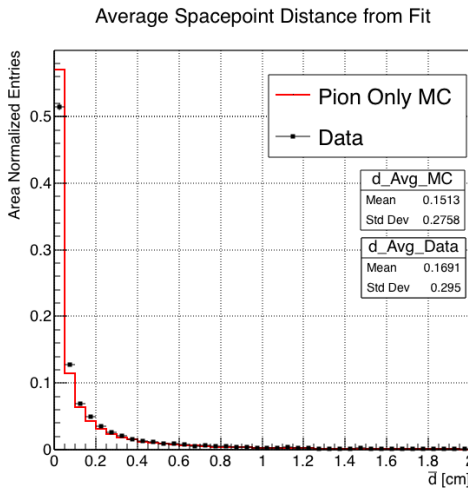


Figure 2.10: Distributions of the average distance between each 3D point in space and the fit line,  $\bar{d}$  for the data used in the pion cross section analysis and the pion only DDMC. The distributions are area normalized.

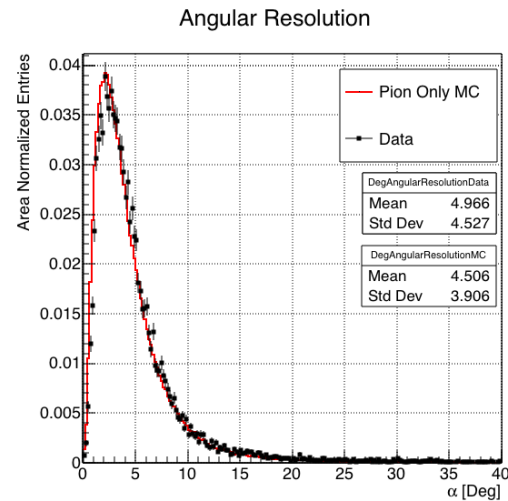


Figure 2.11: Distributions of angular resolution  $\alpha$  for data used in the pion cross section analysis and pion only DDMC. The distributions are area normalized.

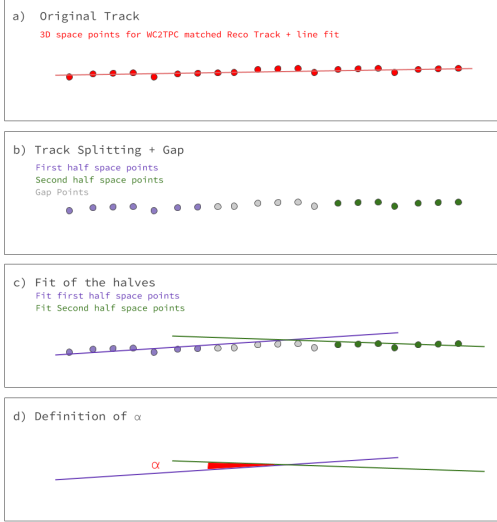


Figure 2.12: A visual representation of the procedure used to evaluate the angular resolution.

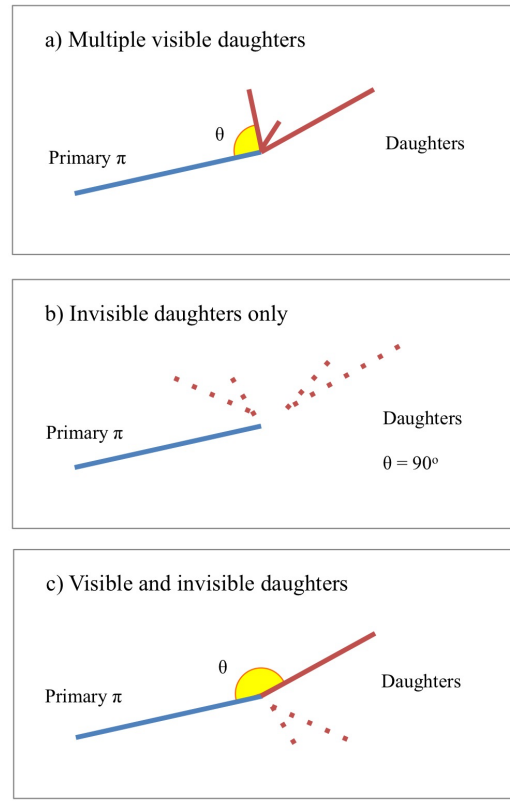


Figure 2.13: A visual representation of the scattering angle definition in case of inelastic scattering.

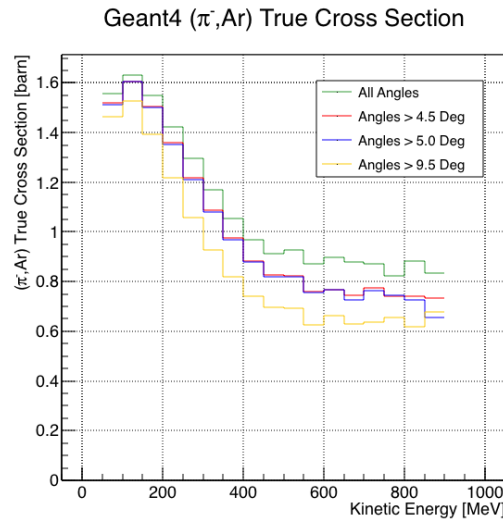


Figure 2.14: True ( $\pi^-$ , Ar) cross section for interaction angles greater than 0 deg (green), 4.5 deg (red), 5.0 deg (blue) and 9.0 deg (yellow).

1056 **2.4 Calorimetry Studies**

1057 The ability to measure the kinetic energy of hadrons in the TPC is fundamental  
1058 for the cross section analyses. Thus, we describe first how we calibrate the TPC  
1059 calorimetric response (Section 2.4.1) and how we measure the kinetic energy of the  
1060 hadrons in the TPC (Section 2.4.2).

1061 **2.4.1 Energy Calibration**

1062 Scope of the energy calibration is to identify the factors which convert the charge  
1063 collected ( $dQ$ ) to energy deposited in the chamber ( $dE$ ). As described in section  
1064 0.1.5, this is a multi-step procedure. In LArIAT, we first correct the raw charge by  
1065 the electronic noise on the considered wire [44], then by the electron lifetime [45],  
1066 and then by the recombination using the ArgoNeut recombination values. Lastly, we  
1067 apply overall calibration of the energy, i.e. we determine the “calorimetry constants”  
1068 using the procedure described in this section.

1069 We independently determine the calorimetry constants for Data and Monte Carlo  
1070 in the LArIAT Run-II Data samples using a parametrization of the stopping power  
1071 (a.k.a. energy deposited per unit length,  $dE/dX$ ) as a function of momentum. This is  
1072 done by comparing the stopping power measured on reconstructed quantities against  
1073 the Bethe-Bloch theoretical prediction for various particle species (see Equation 1).  
1074 We obtain the theoretical expectation for the  $dE/dX$  most probable value of pions  
1075 ( $\pi$ ), muons ( $\mu$ ), kaons ( $K$ ), and protons ( $p$ ) in the momentum range most relevant  
1076 for LArIAT (Figure 2.15) using the tables provided by the Particle Data Group [43]  
1077 for liquid argon [1].

1078 The basic idea of this calibration technique is to utilize a sample of beamline  
1079 events with known particle species and momentum to measure the  $dE/dX$  of the  
1080 corresponding tracks in the TPC. In particular, we decided to use positive pions as

1081 calibration sample and samples from all the other particle species as cross check. Once  
1082 the  $dE/dX$  of the positive pion sample has been measured at various momenta, we  
1083 tune to calorimetry constants within the reconstruction software to align the measured  
1084 values to match the theoretical ones found in Figure 2.15.

1085 In data, we start by selecting a sample of beamline positive pion beamline can-  
1086 didates without any restriction on their measured momentum<sup>2</sup>. We then apply the  
1087 WC2TPC match and subtract the energy loss upstream to the TPC front face, de-  
1088 termining the momentum at the TPC front face. For each surviving pion candidate,  
1089 we measure the  $dE/dx$  at each of the first 12 spacepoints associated the 3D recon-  
1090 structed track, corresponding to a  $\sim 5$  cm portion. These  $dE/dX$  measurements are  
1091 then put into a histogram that corresponds to measured momentum of the track.  
1092 The  $dE/dX$  histograms are sampled every 50 MeV/c in momentum (e.g. 150 MeV/c  
1093  $< P < 200$  MeV/c, 200 MeV/c  $< P < 250$ /c MeV, etc...). This process of selecting,  
1094 sampling, and recording the  $dE/dX$  for various momentum bins is repeated over the  
1095 entire sample of events, allowing us to collect sufficient statistic in most of the mo-  
1096 mentum bins between 150 MeV/c and 1100 MeV/c. On average, pions and muons  
1097 only lose  $\sim 10$  MeV in this 5 cm section of the track and protons lose  $\sim 20$  MeV. Thus  
1098 choosing 50 MeV/c size bins for our histograms covers the energy spread within those  
1099 bins due to energy loss from ionization for all the particle species identifiable in the  
1100 beamline. Each 50 MeV/c momentum binned  $dE/dX$  histogram is now fit with a  
1101 simple Landau function. The most probable value (MPV) and the associated error  
1102 on the MPV from the fit are extracted and plotted against the theoretical prediction  
1103 Figure 2.15. Depending on the outcome of the data-prediction comparison, we modify  
1104 the calorimetry constants and we repeat the procedure until a qualitative agreement  
1105 is achieved. We perform this tuning for the collection and induction plane separately.  
1106 As a cross check to the calorimetry constants determined using the positive pions,

---

2. it should be noted that some muon and position contamination is present in the  $\pi^+$  sample

we lock the constants and plot the  $dE/dx$  versus momentum distribution of all the other particle species identifiable in the beamline data ( $\pi/\mu/e$ , K , p, in both polarities) against the corresponding Beth-Bloch prediction. The agreement between data from the other particle species and the predictions is the expected result of this cross check. The results of the tuning and cross check for Run-II data on the collection plane is shown in Figure 2.16 negative polarity data on top, positive polarity data on the bottom.

In MC, we simulate the corresponding positive pion sample with the DDMC (see section 2.2.2) and follow the same steps as in data. More details on the calorimetry tuning can be found in [33].

1117 Add agreement between data and MC for dedx for pions

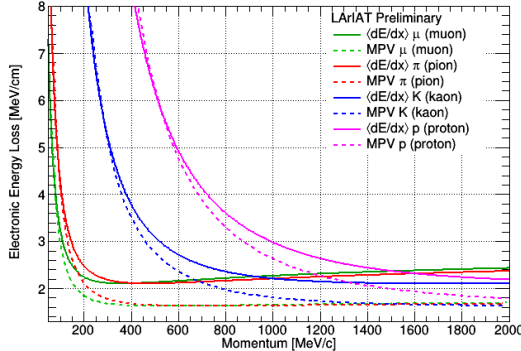


Figure 2.15: Stopping power for pions, muons, kaons, and protons in liquid argon over the momentum range most relevant for LArIAT according to the Beth-Bloch equation. The solid lines represent the prediction for the mean energy  $dE/dX$ , while the dashed lines are the predictions for the MPV.

1118 **2.4.2 Kinetic Energy Measurement**

The measured kinetic energy of a hadron candidate at each argon slab determines which bins of the interacting and incident histograms a selected event is going to fill. In this section, we define the measurement on the kinetic energy and determine the related uncertainty. We will propagate this uncertainty into the cross section

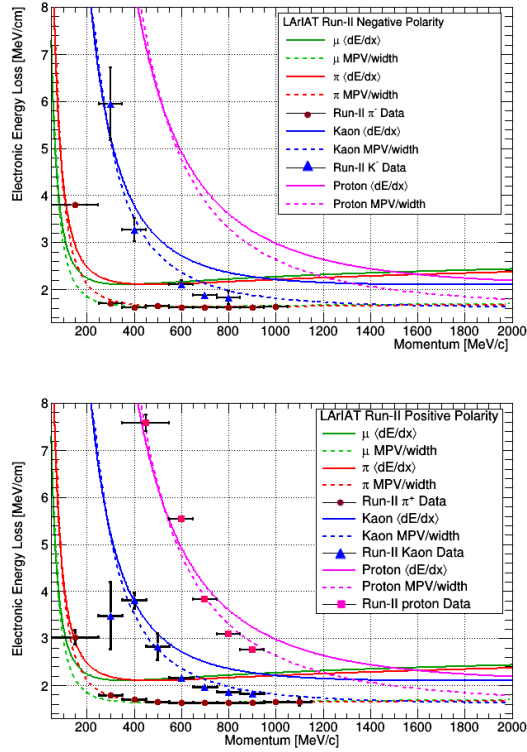


Figure 2.16: Stopping power versus Momentum for Run-II negative (top) and positive (bottom) polarity data. We achieve the agreement between the Bethe-Bloch predictions and the distribution obtained with of the positive pions (top plot, red dots) by tuning the calorimetry constants. Once the calorimetry constants are locked in, the agreement between the other particle species and the Bethe-Bloch predictions follows naturally.

measurement, as discussed in Section 3.1.2 for the pion cross section and in Section ?? for the kaon cross section.

The kinetic energy of a hadron at the  $j^{\text{th}}$  slice of argon in the TPC is given by

$$KE_j = \sqrt{p_{\text{Beam}}^2 + m_{\text{Beam}}^2} - m_{\text{Beam}}^2 - E_{\text{Loss}} - E_{\text{FF-j}}, \quad (2.7)$$

where  $p_{\text{Beam}}$  is the momentum measured by the beamline detectors,  $m_{\text{Beam}}$  is the mass of the hadron as reported in the PDG,  $E_{\text{Loss}}$  is the energy loss between the beamline and the TPC, and  $E_{\text{FF-j}}$  is the energy that the hadron deposited from the

1129 TPC front face until the  $j^{\text{th}}$  slice. The uncertainty on  $KE_j$  is then given by

$$\delta KE_j = \sqrt{\delta p_{Beam}^2 + \delta E_{Loss}^2 + \delta E_{\text{dep FF-j}}^2}, \quad (2.8)$$

1130 where we have dropped the uncertainty on the mass, since it is orders of magnitude  
1131 smaller than the other uncertainties. We assume the relative uncertainty on  $p_{Beam}$  to  
1132 be 2%, and the uncertainty on the energy loss upstream to be 7 MeV, as calculated  
1133 in Section 2.2.3. We describe the estimate of the uncertainty on  $E_{\text{FF-j}}$  in the rest of  
1134 this section.

1135 The energy deposited by the hadron from the TPC front face until the  $j^{\text{th}}$  slice is  
1136 the sum of the measured energy deposited in each previous slabs  $E_i$ , i.e.

$$E_{\text{FF-j}} = \sum_{i < j} E_i, \quad (2.9)$$

1137 where  $E_i$  is measured in each slab as the product of the stopping power,  $dE/dX_i$ ,  
1138 and the track pitch,  $Pitch_i$ , for that point. If we assume conservatively that the  
1139 measurements of  $E_i$  are not independent from one another, the uncertainty on  $E_{\text{FF-j}}$   
1140 becomes

$$\delta E_{\text{FF-j}} = (j - 1)\delta E_i, \quad (2.10)$$

1141 where  $\delta E_i$  is the uncertainty on the energy loss in one slab of argon.

1142 The left side of Figure 2.17 shows the distribution of the energy deposited in each  
1143 slab of argon, for the 60A negative pion dataset in black and for the pion only MC  
1144 in blue. The analogous plot for the -100A negative pion data set is show on the right  
1145 side of Figure 2.17. The distributions are fitted with a landau displayed in red for  
1146 data and in teal for MC. The uncertainty on  $E_i$  is given by the width of the Landau  
1147 fit to the data. A small systematic uncertainty is given by a 1.0% difference between  
1148 the most probable value of the landau fits in data and MC.

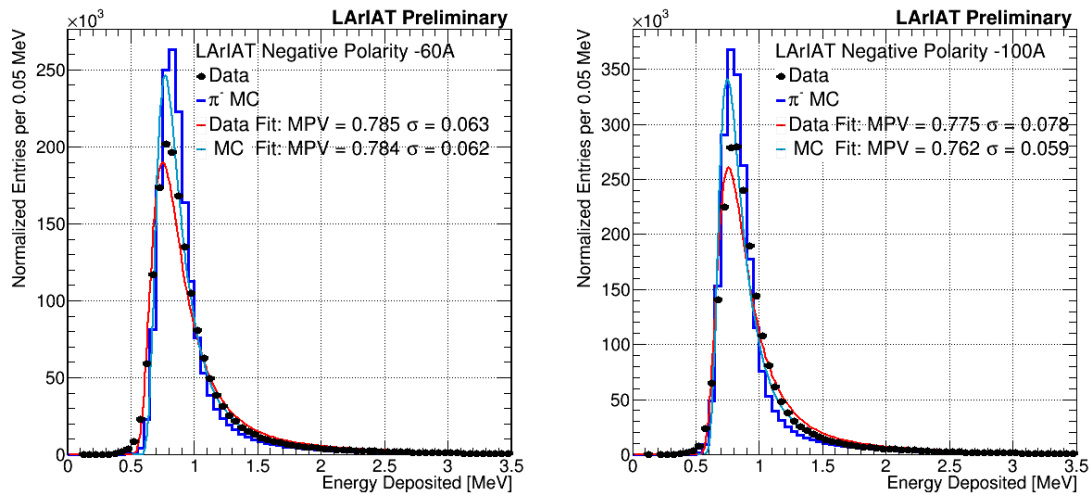


Figure 2.17: Energy deposited  $E_i$  in a single slab of argon for the pion -60A runs (left) and -100A runs (right). The data is shown in black, the MC in blue. The distributions are fitted with a landau displayed in red for data and in teal for MC.

<sub>1149</sub> **Chapter 3**

<sub>1150</sub> **Negative Pion Cross Section**

<sub>1151</sub> **Measurement**

<sub>1152</sub> **3.1 Raw Cross Section**

<sub>1153</sub> We measure the ( $\pi^-$ -Ar) cross section as a function of the kinetic energy in the two  
<sub>1154</sub> chosen data sets, the -60A and -100A negative runs. As we will clarify in Section  
<sub>1155</sub> 3.2, the corrections to the raw cross section depend on the beam conditions and need  
<sub>1156</sub> to be calculated independently for the two data sets. Thus, we present here the  
<sub>1157</sub> measurements on the two datasets separately.

<sub>1158</sub> As stated in section 1.3.2, the raw cross section is given by the equation

$$\sigma_{TOT}(E_i) = \frac{1}{n\delta X} \frac{N_{Int}^{TOT}(E_i)}{N_{Inc}^{TOT}(E_i)}. \quad (3.1)$$

<sub>1159</sub> where  $N_{Int}^{TOT}$  is the number of particles interacting at kinetic energy  $E_i$ ,  $N_{Inc}^{TOT}$  is  
<sub>1160</sub> number of particles incident on an argon slice at kinetic energy  $E_i$ ,  $n$  is the density  
<sub>1161</sub> of the target centers and  $\delta X$  is the thickness of the argon slice.

<sub>1162</sub> Figure 3.1 shows the distribution of  $N_{Int}^{TOT}$  as a function of the kinetic energy for  
<sub>1163</sub> the 60A dataset on the left and for the 100A dataset on the right. The data central

points are represented by black dots, the statistical uncertainty is shown in black, while the systematic uncertainty is shown in red. Data is displayed over the raw cross section obtained with a MC mixed sample of pions, muon and electrons in the percentage predicted by G4Beamline. The contribution from the simulated pions are shown in blue, the ones from secondaries in red, the ones from muons in yellow and the ones from electrons in gray. The simulated pion's and backgrounds' contributions are stacked; the sum of the integrals from each particle species is normalized to the integral of the data.

Figure 3.2 shows the distribution of  $N_{\text{Inc}}^{\text{TOT}}$  for the 60A dataset on the left and for the 100A dataset on the right. Data is displayed over the MC. The same color scheme and normalization procedure is used for both the interacting and incident histograms.

Figure 3.3 shows the raw cross section for the 60A dataset on the left and for the 100A dataset on the right, statistical uncertainty in black and systematic uncertainty in red. The raw data cross section is overlaid to the reconstructed MC cross section (in azure).

The calculation of the statistical uncertainty for the interacting, incident and cross section measurements is laid out in Section 3.1.1, while the corresponding systematics uncertainty on Section 3.1.2.

### 3.1.1 Statistical Uncertainty

The statistical uncertainty for each kinetic energy bin of the cross section plot is calculated by error propagation from the statistical uncertainty on  $N_{\text{Inc}}^{\text{TOT}}$  and  $N_{\text{Int}}^{\text{TOT}}$  correspondent bin. Since the number of incident hadrons in each energy bin is given by a simple counting, we assume that  $N_{\text{Inc}}^{\text{TOT}}$  is distributed as a poissonian with mean and variance equal to  $N_{\text{Inc}}^{\text{TOT}}$  in each bin. On the other hand,  $N_{\text{Int}}^{\text{TOT}}$  follows a binomial distribution: a particle in a given energy bin might or might not interact. The variance

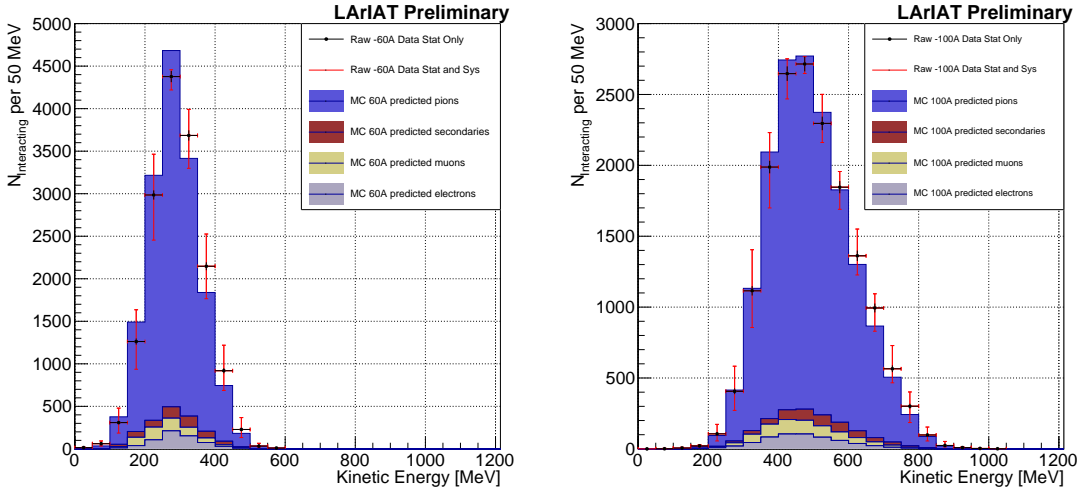


Figure 3.1: Raw number of interacting pion candidates as a function of the reconstructed kinetic energy for the 60A runs (left) and for the 100A runs (right). The statistical uncertainties are shown in black, the systematic uncertainties in red.

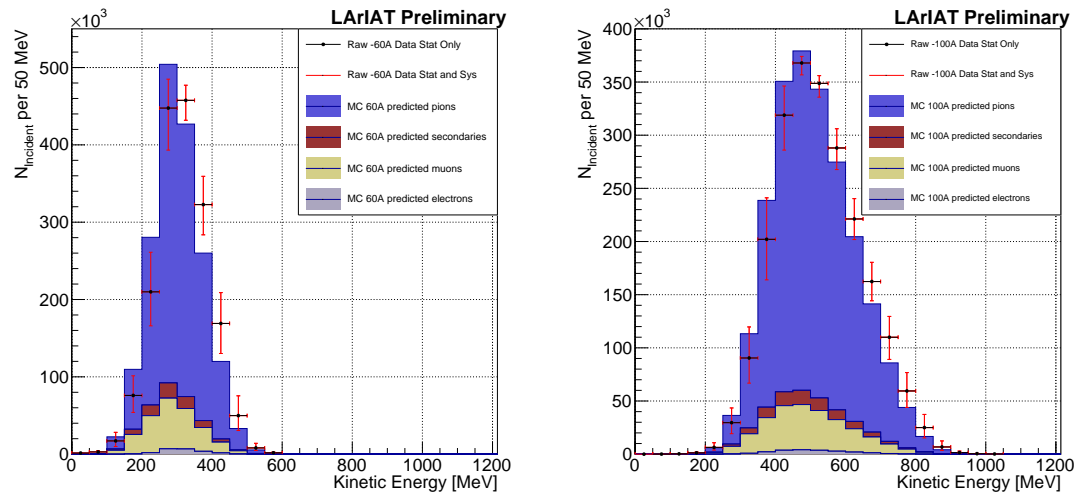


Figure 3.2: Raw number of incident pion candidates as a function of the reconstructed kinetic energy for the 60A runs (left) and for the 100A runs (right). The statistical uncertainties are shown in black, the systematic uncertainties in red.

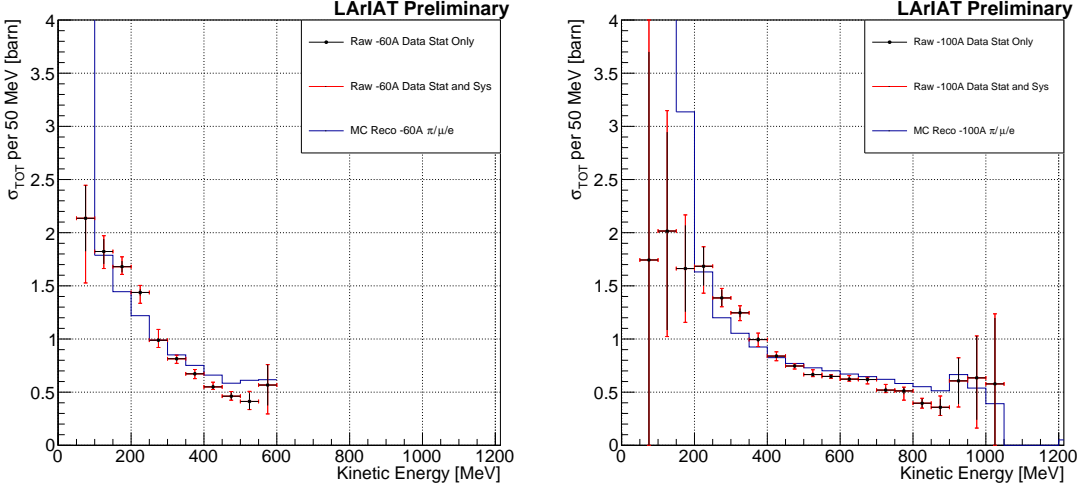


Figure 3.3: Raw ( $\pi^-$ -Ar) total hadronic cross section for the 60A runs (left) and for the 100A runs (right). The statistical uncertainties are shown in black, the systematic uncertainties in red. The raw cross section obtained with a MC mixed sample of pions, muon and electrons in the percentage predicted by G4Beamline is shown in azure.

1189 for the binomial is given by

$$\text{Var}[N_{\text{Int}}^{\text{TOT}}] = \mathcal{N}P_{\text{Interacting}}(1 - P_{\text{Interacting}}); \quad (3.2)$$

1190 since the interaction probability  $P_{\text{Interacting}}$  is  $\frac{N_{\text{Int}}^{\text{TOT}}}{N_{\text{Inc}}^{\text{TOT}}}$  and the number of tries  $\mathcal{N}$  is  
1191  $N_{\text{Inc}}^{\text{TOT}}$ , equation 3.2 translates into

$$\text{Var}[N_{\text{Int}}^{\text{TOT}}] = N_{\text{Inc}}^{\text{TOT}} \frac{N_{\text{Int}}^{\text{TOT}}}{N_{\text{Inc}}^{\text{TOT}}} \left(1 - \frac{N_{\text{Int}}^{\text{TOT}}}{N_{\text{Inc}}^{\text{TOT}}}\right) = N_{\text{Int}}^{\text{TOT}} \left(1 - \frac{N_{\text{Int}}^{\text{TOT}}}{N_{\text{Inc}}^{\text{TOT}}}\right). \quad (3.3)$$

1192  $N_{\text{Inc}}^{\text{TOT}}$  and  $N_{\text{Int}}^{\text{TOT}}$  are not independent. The statistical uncertainty on the cross  
1193 section is thus calculated as

$$\delta\sigma_{\text{tot}}(E) = \sigma_{\text{tot}}(E) \left( \frac{\delta N_{\text{Int}}^{\text{TOT}}}{N_{\text{Int}}^{\text{TOT}}} + \frac{\delta N_{\text{Inc}}^{\text{TOT}}}{N_{\text{Inc}}^{\text{TOT}}} \right) \quad (3.4)$$

1194 where:

$$\delta N_{\text{Inc}}^{\text{TOT}} = \sqrt{N_{\text{Inc}}^{\text{TOT}}} \quad (3.5)$$

$$\delta N_{\text{Int}}^{\text{TOT}} = \sqrt{N_{\text{Int}}^{\text{TOT}} \left(1 - \frac{N_{\text{Int}}^{\text{TOT}}}{N_{\text{Inc}}^{\text{TOT}}}\right)}. \quad (3.6)$$

### 1195 3.1.2 Treatment of Systematics

1196 The only systematic effect considered in the measurement of the raw cross section  
1197 results from the propagation of the uncertainty associate with the measurement of  
1198 the kinetic energy at each slab.

## 1199 3.2 Corrections to the Raw Cross Section

1200 As described in section 1.3.3 as series of corrections are needed to derive the true pion  
1201 cross section from the raw cross section. These corrections are described in equation  
1202 1.9,

$$\sigma_{\text{TOT}}^{\pi^-}(E_i) = \frac{1}{n\delta X} \frac{\epsilon^{\text{Inc}}(E_i)}{\epsilon^{\text{Int}}(E_i)} \frac{C_{\text{Int}}^{\pi MC}(E_i)}{C_{\text{Inc}}^{\pi MC}(E_i)} \frac{N_{\text{Int}}^{\text{TOT}}(E_i)}{N_{\text{Inc}}^{\text{TOT}}(E_i)}. \quad (1.9)$$

### 1203 3.2.1 Background subtraction

#### 1204 Treatment of Systematics

### 1205 3.2.2 Efficiency Correction

#### 1206 Treatment of Systematics

### 1207 3.2.3 Final Plots

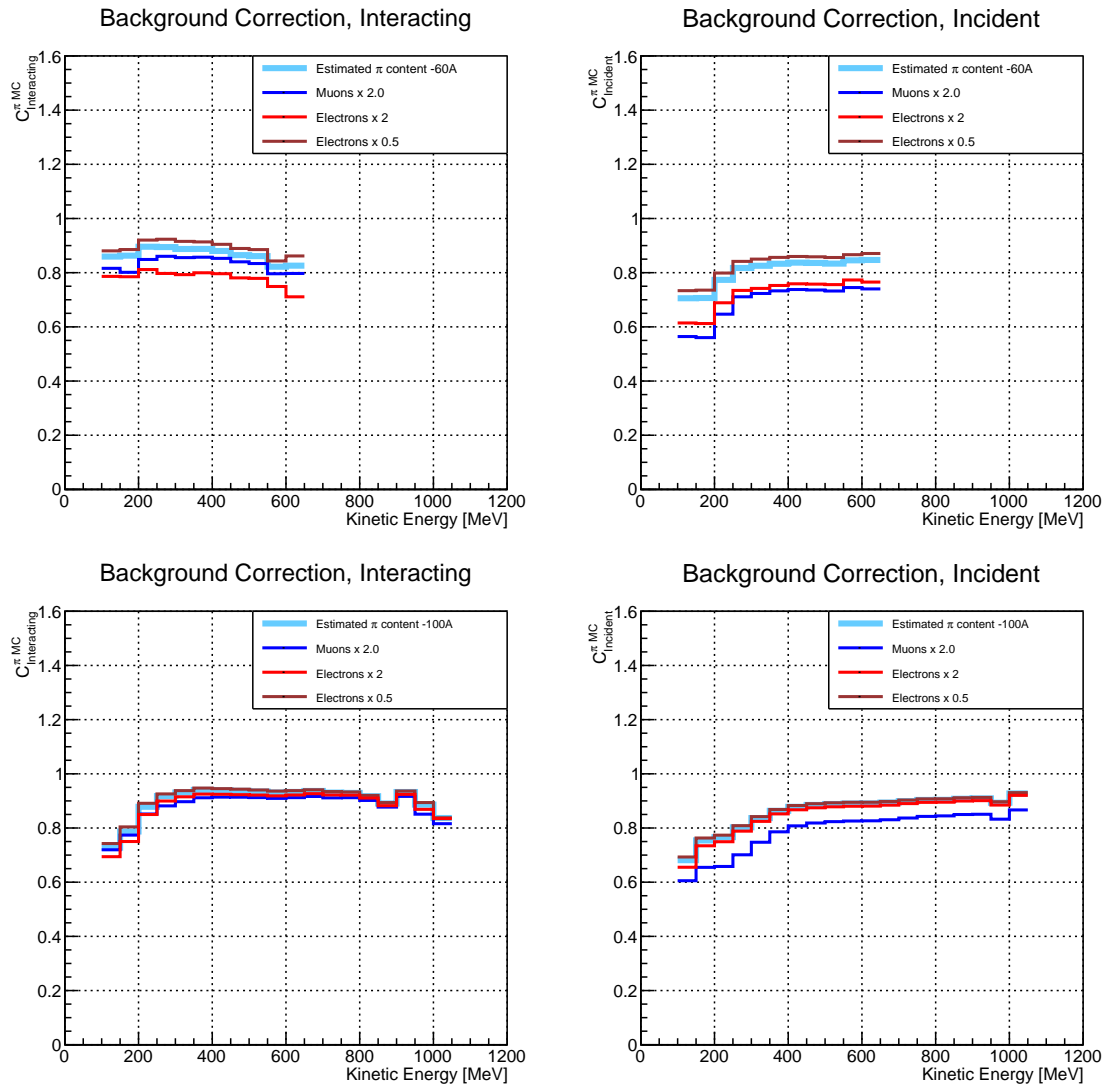


Figure 3.4: .

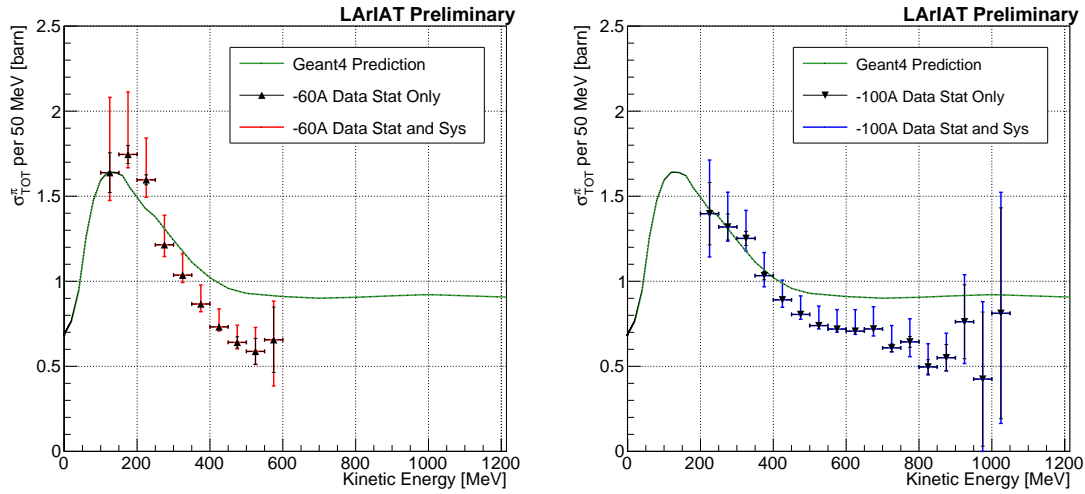


Figure 3.5: .

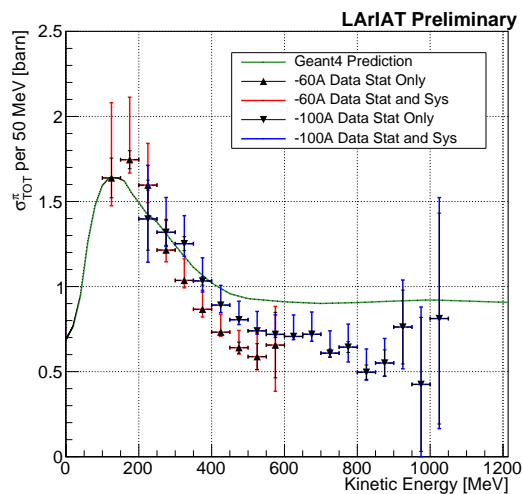


Figure 3.6: .

<sub>1208</sub> **Bibliography**

- <sub>1209</sub> [1] PDG Tables for Liquid Argon. . Technical report.
- <sub>1210</sub> [2] R Acciarri, C Adams, J Asaadi, B Baller, T Bolton, C Bromberg, F Ca-  
<sub>1211</sub> vanna, E Church, D Edmunds, A Ereditato, S Farooq, B Fleming, H Greenlee,  
<sub>1212</sub> G Horton-Smith, C James, E Klein, K Lang, P Laurens, D McKee, R Mehdiyev,  
<sub>1213</sub> B Page, O Palamara, K Partyka, G Rameika, B Rebel, M Soderberg, J Spitz,  
<sub>1214</sub> A M Szelc, M Weber, M Wojcik, T Yang, and G P Zeller. A study of electron  
<sub>1215</sub> recombination using highly ionizing particles in the argoneut liquid argon tpc.  
<sub>1216</sub> *Journal of Instrumentation*, 8(08):P08005, 2013.
- <sub>1217</sub> [3] R Acciarri, M Antonello, B Baibussinov, M Baldo-Ceolin, P Benetti, F Calaprice,  
<sub>1218</sub> E Calligarich, M Cambiaghi, N Canci, F Carbonara, F Cavanna, S Centro, A G  
<sub>1219</sub> Cocco, F Di Pompeo, G Fiorillo, C Galbiati, V Gallo, L Grandi, G Meng, I Mod-  
<sub>1220</sub> ena, C Montanari, O Palamara, L Pandola, G B Piano Mortari, F Pietropaolo,  
<sub>1221</sub> G L Raselli, M Roncadelli, M Rossella, C Rubbia, E Segreto, A M Szelc, S Ven-  
<sub>1222</sub> tura, and C Vignoli. Effects of nitrogen contamination in liquid argon. *Journal*  
<sub>1223</sub> *of Instrumentation*, 5(06):P06003, 2010.
- <sub>1224</sub> [4] R. Acciarri et al. Design and Construction of the MicroBooNE Detector. *JINST*,  
<sub>1225</sub> 12(02):P02017, 2017.
- <sub>1226</sub> [5] R. Acciarri et al. First Observation of Low Energy Electron Neutrinos in a Liquid  
<sub>1227</sub> Argon Time Projection Chamber. *Phys. Rev.*, D95(7):072005, 2017. [Phys.

- 1228 Rev.D95,072005(2017)].
- 1229 [6] M Adamowski, B Carls, E Dvorak, A Hahn, W Jaskierny, C Johnson, H Jostlein,  
1230 C Kendziora, S Lockwitz, B Pahlka, R Plunkett, S Pordes, B Rebel, R Schmitt,  
1231 M Stancari, T Tope, E Voirin, and T Yang. The liquid argon purity demonstrator.  
1232 *Journal of Instrumentation*, 9(07):P07005, 2014.
- 1233 [7] C. Adams et al. The Long-Baseline Neutrino Experiment: Exploring Fundamen-  
1234 tal Symmetries of the Universe. 2013.
- 1235 [8] Alan Agresti. *Categorical Data Analysis*. Wiley Series in Probability and Statis-  
1236 tics. Wiley, 2013.
- 1237 [9] A. Aguilar-Arevalo et al. Evidence for neutrino oscillations from the observa-  
1238 tion of anti-neutrino(electron) appearance in a anti-neutrino(muon) beam. *Phys.*  
1239 *Rev.*, D64:112007, 2001.
- 1240 [10] A. A. Aguilar-Arevalo et al. Improved Search for  $\bar{\nu}_\mu \rightarrow \bar{\nu}_e$  Oscillations in the  
1241 MiniBooNE Experiment. *Phys. Rev. Lett.*, 110:161801, 2013.
- 1242 [11] S. Amoruso et al. Study of electron recombination in liquid argon with the  
1243 ICARUS TPC. *Nucl. Instrum. Meth.*, A523:275–286, 2004.
- 1244 [12] C. Anderson et al. The ArgoNeuT Detector in the NuMI Low-Energy beam line  
1245 at Fermilab. *JINST*, 7:P10019, 2012.
- 1246 [13] M. Antonello, B. Baibussinov, P. Benetti, E. Calligarich, N. Canci, S. Cen-  
1247 tro, A. Cesana, K. Cieslik, D. B. Cline, A. G. Cocco, A. Dabrowska, D. De-  
1248 qual, A. Dermenev, R. Dolfini, C. Farnese, A. Fava, A. Ferrari, G. Fiorillo,  
1249 D. Gibin, S. Gninenko, A. Guglielmi, M. Haranczyk, J. Holeczek, A. Ivashkin,  
1250 J. Kisiel, I. Kochanek, J. Lagoda, S. Mania, A. Menegolli, G. Meng, C. Monta-  
1251 nari, S. Otwinowski, A. Piazzoli, P. Picchi, F. Pietropaolo, P. Plonski, A. Rap-

- 1252 poldi, G. L. Raselli, M. Rossella, C. Rubbia, P. Sala, A. Scaramelli, E. Seg-  
1253 reto, F. Sergiampietri, D. Stefan, J. Stepaniak, R. Sulej, M. Szarska, M. Ter-  
1254 rani, F. Varanini, S. Ventura, C. Vignoli, H. Wang, X. Yang, A. Zalewska, and  
1255 K. Zaremba. Precise 3d track reconstruction algorithm for the ICARUS t600 liq-  
1256 uid argon time projection chamber detector. *Advances in High Energy Physics*,  
1257 2013:1–16, 2013.
- 1258 [14] M. Antonello et al. A Proposal for a Three Detector Short-Baseline Neutrino  
1259 Oscillation Program in the Fermilab Booster Neutrino Beam. 2015.
- 1260 [15] C. Athanassopoulos et al. Evidence for  $\nu(\mu) \rightarrow \nu(e)$  neutrino oscillations  
1261 from LSND. *Phys. Rev. Lett.*, 81:1774–1777, 1998.
- 1262 [16] B. Baller. Trajcluster user guide. Technical report, apr 2016.
- 1263 [17] Gary Barker. Neutrino event reconstruction in a liquid argon TPC. *Journal of*  
1264 *Physics: Conference Series*, 308:012015, jul 2011.
- 1265 [18] J B Birks. Scintillations from organic crystals: Specific fluorescence and relative  
1266 response to different radiations. *Proceedings of the Physical Society. Section A*,  
1267 64(10):874, 1951.
- 1268 [19] Mark G. Boulay and A. Hime. Direct WIMP detection using scintillation time  
1269 discrimination in liquid argon. 2004.
- 1270 [20] W. M. Burton and B. A. Powell. Fluorescence of tetraphenyl-butadiene in the  
1271 vacuum ultraviolet. *Applied Optics*, 12(1):87, jan 1973.
- 1272 [21] E. Church. LArSoft: A Software Package for Liquid Argon Time Projection Drift  
1273 Chambers. 2013.
- 1274 [22] The LArIAT Collaboration. The liquid argon in a testbeam (lariat) experiment.  
1275 Technical report, In Preparation 2018.

- 1276 [23] S.E. Derenzo, A.R. Kirschbaum, P.H. Eberhard, R.R. Ross, and F.T. Solmitz.  
1277       Test of a liquid argon chamber with 20 m rms resolution. *Nuclear Instruments*  
1278       and Methods, 122:319 – 327, 1974.
- 1279 [24] A Ereditato, C C Hsu, S Janos, I Kreslo, M Messina, C Rudolf von Rohr, B Rossi,  
1280       T Strauss, M S Weber, and M Zeller. Design and operation of argontube: a 5 m  
1281       long drift liquid argon tpc. *Journal of Instrumentation*, 8(07):P07002, 2013.
- 1282 [25] R. Acciarri et al. Convolutional neural networks applied to neutrino events  
1283       in a liquid argon time projection chamber. *Journal of Instrumentation*,  
1284       12(03):P03011, 2017.
- 1285 [26] R. Acciarri et al. Design and construction of the MicroBooNE detector. *Journal*  
1286       of *Instrumentation*, 12(02):P02017–P02017, feb 2017.
- 1287 [27] C. E. Aalseth et al.l. DarkSide-20k: A 20 tonne two-phase LAr TPC for direct  
1288       dark matter detection at LNGS. *The European Physical Journal Plus*, 133(3),  
1289       mar 2018.
- 1290 [28] V.M. Gehman, S.R. Seibert, K. Rielage, A. Hime, Y. Sun, D.-M. Mei, J. Maassen,  
1291       and D. Moore. Fluorescence efficiency and visible re-emission spectrum of  
1292       tetraphenyl butadiene films at extreme ultraviolet wavelengths. *Nuclear Instru-*  
1293       *ments and Methods in Physics Research Section A: Accelerators, Spectrometers,*  
1294       *Detectors and Associated Equipment*, 654(1):116 – 121, 2011.
- 1295 [29] H. Geiger and E. Marsden. On a diffuse reflection of the formula-particles. *Pro-*  
1296       *ceedings of the Royal Society A: Mathematical, Physical and Engineering Sci-*  
1297       *ences*, 82(557):495–500, jul 1909.
- 1298 [30] C. Green, J. Kowalkowski, M. Paterno, M. Fischler, L. Garren, and Q. Lu. The  
1299       Art Framework. *J. Phys. Conf. Ser.*, 396:022020, 2012.

- 1300 [31] H J Hilke. Time projection chambers. *Reports on Progress in Physics*,  
1301 73(11):116201, 2010.
- 1302 [32] N. Ishida, M. Chen, T. Doke, K. Hasuike, A. Hitachi, M. Gaudreau, M. Kase,  
1303 Y. Kawada, J. Kikuchi, T. Komiya, K. Kuwahara, K. Masuda, H. Okada, Y.H.  
1304 Qu, M. Suzuki, and T. Takahashi. Attenuation length measurements of scintil-  
1305 lation light in liquid rare gases and their mixtures using an improved reflection  
1306 suppresser. *Nuclear Instruments and Methods in Physics Research Section A: Accelerators, Spectrometers, Detectors and Associated Equipment*, 384(2-3):380–  
1307 386, jan 1997.
- 1309 [33] G. Pulliam J. Asaadi, E. Gramellini. Determination of the electron lifetime in  
1310 lariat. Technical report, August 2017.
- 1311 [34] George Jaffé. Zur theorie der ionisation in kolonnen. *Annalen der Physik*,  
1312 347(12):303–344, 1913.
- 1313 [35] B J P Jones, C S Chiu, J M Conrad, C M Ignarra, T Katori, and M Toups.  
1314 A measurement of the absorption of liquid argon scintillation light by dissolved  
1315 nitrogen at the part-per-million level. *Journal of Instrumentation*, 8(07):P07011,  
1316 2013.
- 1317 [36] Benjamin J. P. Jones. *Sterile Neutrinos in Cold Climates*. PhD thesis, MIT,  
1318 2015.
- 1319 [37] M A Leigui de Oliveira. Expression of Interest for a Full-Scale Detector Engi-  
1320 neering Test and Test Beam Calibration of a Single-Phase LAr TPC. Technical  
1321 Report CERN-SPSC-2014-027. SPSC-EOI-011, CERN, Geneva, Oct 2014.
- 1322 [38] W. H. Lippincott, K. J. Coakley, D. Gastler, A. Hime, E. Kearns, D. N. McK-  
1323 insey, J. A. Nikkel, and L. C. Stonehill. Scintillation time dependence and pulse  
1324 shape discrimination in liquid argon. *Phys. Rev. C*, 78:035801, Sep 2008.

- 1325 [39] M. Mooney. The microboone experiment and the impact of space charge effects.  
1326 2015.
- 1327 [40] E. Morikawa, R. Reininger, P. Gürtler, V. Saile, and P. Laporte. Argon, krypton,  
1328 and xenon excimer luminescence: From the dilute gas to the condensed phase.  
1329 *The Journal of Chemical Physics*, 91(3):1469–1477, aug 1989.
- 1330 [41] D. R. Nygren. The time projection chamber: A new  $4\pi$  detector for charged  
1331 particles. Technical report, 1974.
- 1332 [42] L. Onsager. Initial recombination of ions. *Phys. Rev.*, 54:554–557, Oct 1938.
- 1333 [43] C. Patrignani et al. Review of Particle Physics. *Chin. Phys.*, C40(10):100001,  
1334 2016.
- 1335 [44] T. Yang R. Acciarri. Investigation of the non-uniformity observed in the wire  
1336 response to charge in lariat run 1. Technical report, February 2017.
- 1337 [45] T. Yang R. Acciarri, M. Stancari. Determination of the electron lifetime in lariat.  
1338 Technical report, March 2016.
- 1339 [46] C. Rubbia. The Liquid Argon Time Projection Chamber: A New Concept for  
1340 Neutrino Detectors. 1977.
- 1341 [47] R. K. Teague and C. J. Pings. Refractive index and the lorentz–lorenz function  
1342 for gaseous and liquid argon, including a study of the coexistence curve near the  
1343 critical state. *The Journal of Chemical Physics*, 48(11):4973–4984, jun 1968.
- 1344 [48] J. Thomas and D. A. Imel. Recombination of electron-ion pairs in liquid argon  
1345 and liquid xenon. *Phys. Rev. A*, 36:614–616, Jul 1987.
- 1346 [49] N Yahlali, L M P Fernandes, K Gonzlez, A N C Garcia, and A Soriano. Imaging  
1347 with sipms in noble-gas detectors. *Journal of Instrumentation*, 8(01):C01003,  
1348 2013.